

Contents lists available at ScienceDirect

Bioactive Materials

journal homepage: www.keaipublishing.com/en/journals/bioactive-materials





Shape memory bone screws loading L-arginine and Ca²⁺ propagate mechanical stimulation, energize bone cells and augment bone regeneration

Huaqian Liu^{a,1}, Weiwei Zhao^{b,c,1}, Yuhe Yang^{a,1}, Ho-Pan Bei^a, Qunchao Chen^d, Xintong Zhou^a, Yuanchi Zhang^e, Chunyi Wen^f, Yuefeng Hao^d, Jinlian Hu^g, Yaxiong Liu^{h,i}, Yu Zhang^j, Ka-Hing Wong^k, Hongyu Zhang^{c,*}, Xin Zhao^{a,**}

- a Department of Applied Biology and Chemical Technology, The Hong Kong Polytechnic University, Hung Hom, Kowloon, Hong Kong SAR, 999077, China
- b Department of Biomaterials, School and Hospital of Stomatology, Cheeloo College of Medicine, Shandong University & Shandong Key Laboratory of Oral Tissue Regeneration & Shandong Engineering Research Center of Dental Materials and Oral Tissue Regeneration & Shandong Provincial Clinical Research Center for Oral Diseases, Jinan, Shandong, 250012, China
- c State Key Laboratory of Tribology in Advanced Equipment, Department of Mechanical Engineering, Tsinghua University, Beijing, 100084, China
- ^d Orthopedics and Sports Medicine Center, The Affiliated Suzhou Hospital of Nanjing Medical University, 215006, China
- e Centre for Translational Medicine Research & Development, Shenzhen Institute of Advanced Technology, Chinese Academy of Sciences, Shenzhen, 518055, China
- f Department of Biomedical Engineering, the Hong Kong Polytechnic University, Hung Hom, Kowloon, Hong Kong SAR, 999077, China
- g Department of Biomedical Engineering, City University of Hong Kong, Hong Kong SAR., 999077, China
- ^h School of Mechatronic Engineering and Automation, Foshan University, Foshan, 528225, China
- i Ji Hua Laboratory, Foshan, 528200, China
- ^j Medical Research Center, Department of Orthopedics, Guangdong Provincial People's Hospital, Guangdong Academy of Medical Sciences, Guangzhou 510080, China
- ^k Research Institute for Future Food, Department of Food Science and Nutrition, The Hong Kong Polytechnic University, Hung Hom, Kowloon, Hong Kong SAR, 999077, China

ARTICLE INFO

Keywords: Bone screws Shape memory effect NO-cGMP signaling pathway Calcium signaling pathway Osteogenesis-angiogenesis coupling

ABSTRACT

Metallic bone screws are clinically used to fix the fractured bone fragments in bone defect treatment; yet they present compromised therapeutic efficacy due to poor osseointegration and tissue support. Here, we develop a novel thermoresponsive shape memory (SMP) bone screw with osteogenesis-angiogenesis coupling for enhanced bone regeneration. The SMP bone screws are prepared by die casting of shape memory polyurethane/hydroxyapatite (PU/HA) composite, coated with L-arginine (Arg) and calcium ions (Ca²⁺). The SMP bone screw could shrink and be easily reshaped at room temperature (25°C) and then rapidly recover to its original state (37°C), granting it robust internal fixation capacity (2-fold increase in pull-out force) and beneficial compressive force to nearby tissues. Additionally, the long-term release of L-arginine and calcium ions synergistically activate the nitric oxide-cyclic guanosine monophosphate (NO-cGMP) signaling pathway of native cells. Synergized with its shape memory function, the SMP bone screw activated calcium signaling pathway under the stimulation of mechanical stress, promote the activation of various osteogenic pathways (e.g. P13K-Akt signaling pathway), and upregulate the NO-cGMP pathway by regulating the influx of calcium ions and arginine to synchronously coordinate osteogenesis and angiogenesis to accelerate bone repair. We envision that our slot-in, snap-back and homeothermal shape memory bone screw, with its easily reshaped and fast stress release properties and osteogenesis-angiogenesis coupling efficacy, can shed new light on the development of clinical bone screws.

Peer review under the responsibility of editorial board of Bioactive Materials.

E-mail addresses: zhanghyu@tsinghua.edu.cn (H. Zhang), xin.zhao@polyu.edu.hk (X. Zhao).

https://doi.org/10.1016/j.bioactmat.2025.07.007

Received 14 January 2025; Received in revised form 1 July 2025; Accepted 3 July 2025 Available online 18 July 2025

^{*} Corresponding author.

^{**} Corresponding author.

¹ These authors contributed equally to this work.

1. Introduction

Bone screws play a pivotal role in modern orthopedic surgery by providing essential mechanical support for bone stabilization and facilitating the bone healing process [1]. Despite the widespread use of conventional bone screws which are predominantly made from metals (e.g., titanium and stainless steel), they present several challenges such as the potential for causing tissue damage and the risk of loosening over time [2,3] and stress shielding [4-6], which can limit their effectiveness and application in clinical settings. Recently, shape memory materials have been applied in the preparation of bone screws that can be pre-compressed during insertion to minimize tissue damage, and subsequently revert to their original shape when exposed to specific stimuli temperature and moisture). programmable (e.g., Such contraction-expansion characteristic endows bone screws made of shape memory materials with a tight-fitting assimilation between the material and surrounding tissues, thereby reducing the likelihood of loosening or

dislodgement [7,8]. Yet shape memory bone screws often necessitate harsh conditions to activate their shape memory effect. For instance, polylactic acid (PLA)-based shape memory bone screws typically require temperatures exceeding 45°C to revert to their original shape, posing a serious risk of thermal damage to surrounding tissues [9-13]. More importantly, the current design of shape memory bone screws did not account for favorable biomechanical factors (e.g., compressive stress) which can significantly modulate cellular metabolism and activate mechanosensitive signaling pathways such as phosphatidylinositol 3-Kinase/Protein Kinase B (PI3K/Akt) signaling pathway to expedite bone reconstruction [14,15]. Additionally, our previous studies have shown that biochemical factors (e.g., nitric oxide) can energize bone and vascular during bone healing osteogenesis-angiogenesis, which is paramount for the comprehensive integration and long-term success of bone screws [16,17,18]. However, the mutual coordination of the biomechanical and biochemical microenvironment of shape memory bone screws for enhanced orthopedic

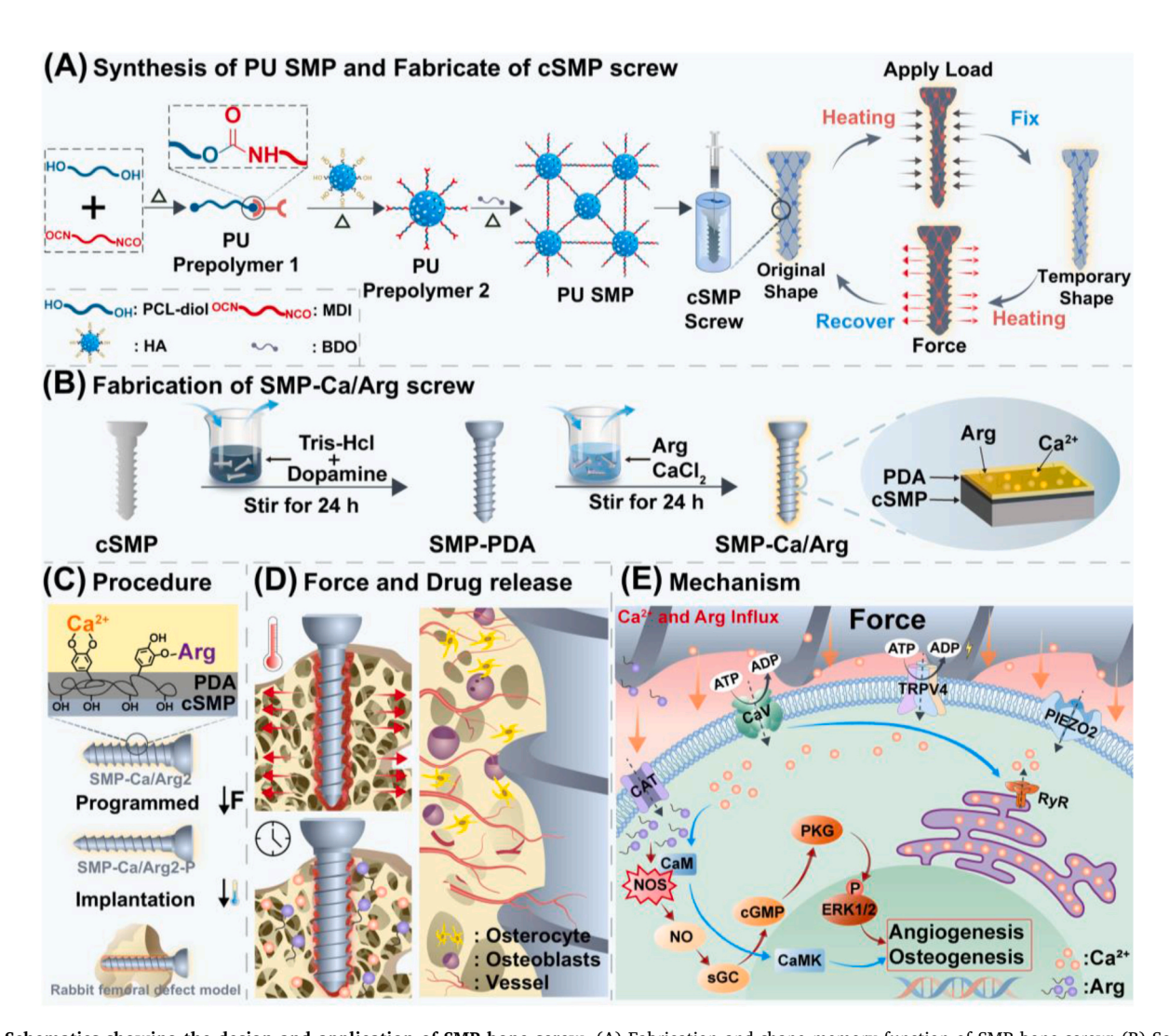


Fig. 1. Schematics showing the design and application of SMP bone screw. (A) Fabrication and shape memory function of SMP bone screw; (B) Schematic illustration of preparation process of SMP-Ca/ArgX (X = 0.5, 1, 2) bone screw; (C) Dopamine-assisted coating of Ca^{2+} and Arg's SMP-Ca/Arg screw and subsequent implantation into the bone defect site; (D) SMP-Ca/Arg-P bone screw (an SMP bone screw coated with PDA, Ca^{2+} , and 2.0 mg/mL of Arg, and then compressed) can release mechanical force and Ca^{2+} for coupled osteogenesis-angiogenesis in bone repair; (E) Schematic illustration of the forces activate the mechanosensitive transient receptor potential vanilloid 4 (TRPV4) protein and piezo type mechanosensitive ion channel component 2 (PIEZO2). This activation boosts adenosine triphosphate (ATP) generation and enhancing cellular metabolism, facilitating the influx of Ca^{2+} and Arg released by the SMP-Ca/Arg bone screws through activated calcium channels (e.g., TRPV4 and PIEZO2) and cell membrane proteins (e.g., cationic amino acid transporter (CAT)). The elevated Ca^{2+} level further upregulates calmodulin (CaM) and increase the activity of nitric oxide synthase (NOS) for Arg decomposition to regenerate nitric oxide (NO). This subsequently activates the NO-cGMP pathway, promoting coupled osteogenesis and angiogenesis. The calcium signaling pathway is visually represented by blue arrows, the NO-cGMP pathway is represented by red arrows, and the forces exerted by the SMP-Ca/Arg-P bone screw is indicated by orange arrows.

treatments has been scarcely reported owing to the difficulty to accommodate the biomechanical-biochemical signals within a highly delicate yet dynamic setting of bone fixture [19]. The bone screw serves beyond fixation, necessitating consideration of regenerative needs to minimize secondary damage during implantation, and further enhance

mechanical stimulation and synergistic biochemical signals to enhance cell signal conversion for promoting bone repair.

Here, we fabricated bone screws by die casting a shape memory polyurethane/hydroxyapatite (PU/HA) composite, referred to as control-naked-SMP (cSMP). Subsequently, the cSMP bone screws were

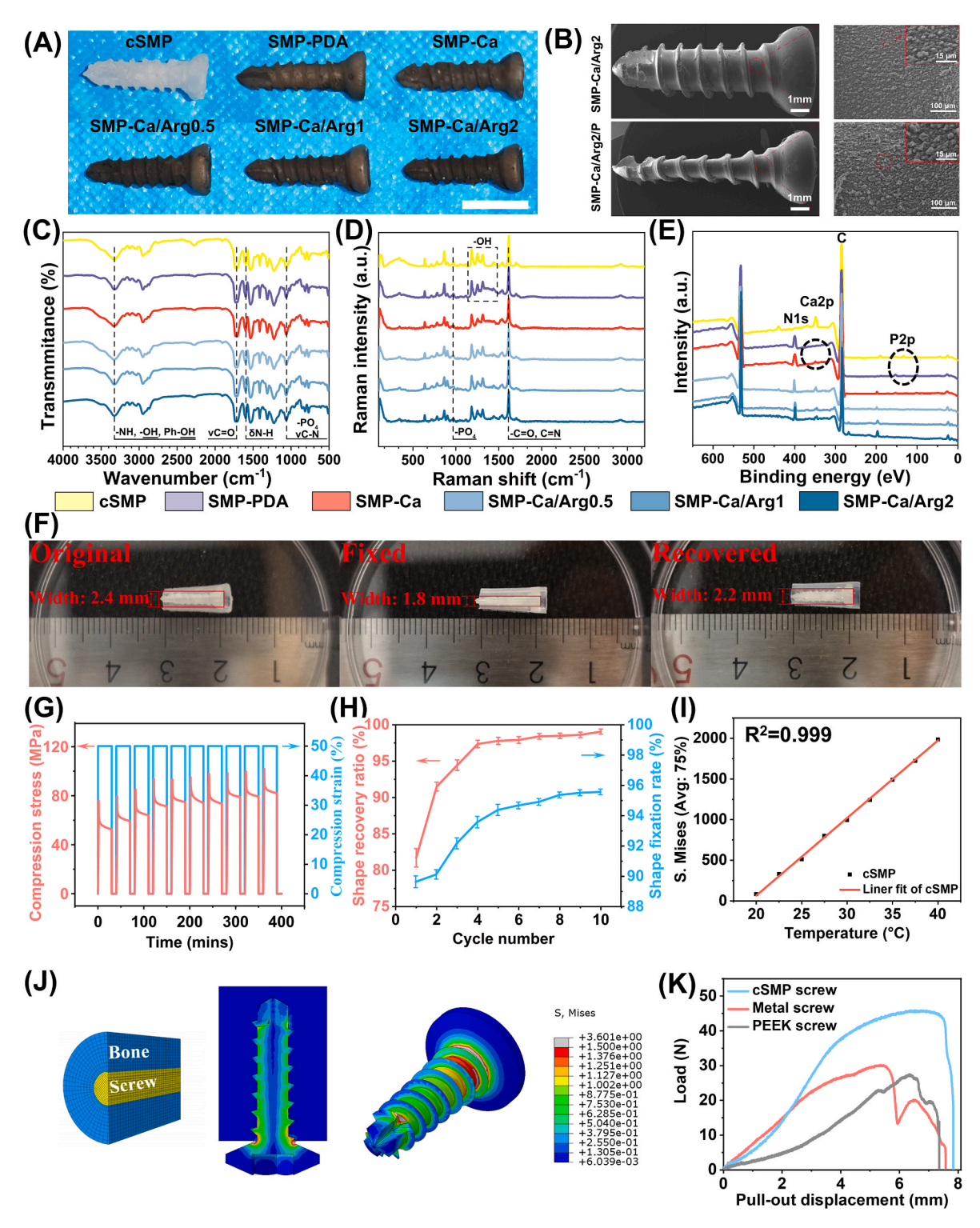


Fig. 2. Structural, mechanical properties and shape memory behaviors of the developed SMP bone screws. (A) Images showing SMP bone screws (scale bar: 1 cm); (B) SEM images showing the surface of SMP-Ca/Arg2 screw before and after compression for 10 times; FTIR spectra (C), Raman spectra (D), and XPS spectra (E) of different SMP bone screws; (F) The shape recovery process of SMP screw; (G) Repeated compressive performance of SMP screw; (H) Shape recovery and fixation rate of SMP screw; (I) The linear curve of stress with temperature by finite element analysis; (J) Equivalent stress distribution by finite element analysis under torsional forces; (K) The excellent pull-out test results of SMP screw compared with metal screw and PEEK screw.

coated with L-arginine (Arg) and calcium ions (Ca²⁺), yielding the SMP-Ca/Arg bone screws. Such design is to propagate biomechanical stimulation and energize bone cells for augmented bone regeneration (Fig. 1). We adopt the polycaprolactone-diol (PCL-diol), 4,4-methylenebis (phenyl isocyanate) (MDI), 1,4-butanediol (BDO) and hydroxyapatite (HA) as the cSMP basal materials (Fig. 1A). The HA was adopted due to its structural similarity to natural bone for enhanced osteoconductive and osteoinductive properties. Moreover, we have previously demonstrated that HA could also significantly improve the mechanical properties of the PU (e.g., including stiffness and recovery stress) for achieving reliable shape memory performance [19]. We demonstrate such thermally responsive SMP exhibits excellent biocompatibility and can revert to its original shape at body temperature (37°C) with high deformation capability. Moreover, it can be easily fabricated into bone screws using a simple die-casting process. Subsequently, we immobilize the Arg/Ca²⁺ onto the cSMP bone screws in dopamine solution through chelation and covalent interactions to prepare the SMP-Ca/Arg bone screws (Fig. 1B). Our SMP-Ca/Arg bone screws can be pre-compressed at 60°C with 50% strain to minimize tissue damage during insertion, while expanding at body temperature (99.5% recovery rate at 37°C) to facilitate implementation and ensure robust fixation (Fig. 1C). After implantation in rabbit femoral defect model, our SMP-Ca/Arg bone screws exert substantial compressive stress (~80 MPa) onto the surrounding bone tissue and demonstrate the capability to modulate biomechanical and biochemical signaling through the coordinated activation of mechanosensitive membrane proteins, cell energy metabolism, calcium channels and nitric oxide synthase (NOS) activity, leading to enhanced osteogenesis-angiogenesis coupling (Fig. 1D).

To the best of our knowledge, this is the first study to elucidate the synergistic regulatory mechanism of the biomechanical forces generated during the shape memory process and the biochemical cues provided by surface-adhered L-arginine (Arg) and Ca²⁺. This biomechanical and biochemical synergy promotes bone healing by enhancing both osteogenesis and angiogenesis, which are paramount for effective bone regeneration. Specifically, this work highlights the role of biomechanical forces in creating a favorable microenvironment for bone cells, while also demonstrating how the biochemical microenvironment, through Arg/Ca²⁺, can stimulate cell metabolism and NO production for osteogenesis-angiogenesis coupling (Fig. 1E). Such synergistic biomechanical and biochemical regulation has never been studied before in the context of shape memory bone screws. We envision that our proposed SMP-Ca/Arg bone screws not only serve as fast-fixing, tightfitting, and cell-stimulating restorative implants but also offer a novel strategy for designing next-generation bone screws for the treatment of bone defects. Additionally, the synergistic working principles uncovered in this study have significant implications for other conditions, such as osteoarthritis and bone tumors, where enhanced bone regeneration and vascularization are essential for successful treatment outcomes.

2. Results and discussion

2.1. Synthesis and characteristics of SMP bone screws

Characteristics of SMP bone screws were illustrated in Fig. 2. Compared with the control naked bone screws made of PU/HA (cSMP), the cSMP bone screw coated with PDA (SMP-PDA), with PDA and Ca $^{2+}$ (SMP-Ca), with PDA, Ca $^{2+}$ and 0.5 mg/mL of Arg (SMP-Ca/Arg0.5), with PDA, Ca $^{2+}$ and 1.0 mg/mL of Arg (SMP-Ca/Arg1), and with PDA, Ca $^{2+}$ and 2.0 mg/mL of Arg (SMP-Ca/Arg2) showed distinct color change owing to the oxidation of dopamine during the coating process (Fig. 2A). PDA coating and Arg immobilization significantly improved the hydrophilic properties of the SMP materials with the water contact angle decreasing from 87.1° to 19.6°, which facilitated the release of Arg adhered to the surface of the SMP bone screw (Fig. S1A). The SEM images of the SMP bone screws in Fig. S1B presented a uniform and dense coating of Ca $^{2+}$ and Arg. We then performed a systematic

circumferential compressive process to make the SMP bone screws slimmer. This was achieved by heating the screws to 60°C, applying radial compressive force, and subsequently cooling them to lock their temporary shape (25°C). To evaluate the shape memory effect, the compressed samples were heated to 37°C (body temperature). Notably, the SMP-Ca/Arg2 bone screw could withstand at least ten repeated compressions without compromising its mechanical strength and coating integrity (Fig. 2B).

The FTIR spectra revealed notable changes in the different SMP materials (Fig. 2C). The characteristic wide and small -OH stretching peak at 3300 cm⁻¹ in the composites confirmed the successful PDA coating. Furthermore, the decreased absorption band intensities of C-N and C=O at 1161 cm⁻¹ and 1721 cm⁻¹ proved the formation of new ester bonds because Arg successfully adhered to the surface of polydopamine. The Raman spectra complemented the FTIR analysis, confirming structural aspects of the different SMP materials (Fig. 2D). The 1056 cm⁻¹ band corresponded to the vibrations of PO₄³⁻ and C-N in the PU and HA domain. The 1610 cm⁻¹ band represented vibrations of C=O and C=N in Arg, while the wide peak at 1350 cm⁻¹ indicated vibrations of -OH in the PDA coating. The SMP composite groups exhibit characteristic peaks at 1056, 1350, and 1610 cm⁻¹, indicating the successful preparation of Arg-coated SMP-Ca/Arg. Furthermore, XPS results offered insight into the elemental compositions of different SMP materials (Fig. 2E). The presence of Ca2p (347.8 eV) and P2p (131.3 eV) peaks in the SMP confirmed successful HA doping (Figs. S2 and S3). An increased N1s peak (399.3 eV) confirmed dopamine adhesion onto the SMP (Fig. S4). The immobilization of Ca²⁺ and Arg was evident from the reappearance of the Ca2p peak (348.9 eV) and an increase in the N1s peak (398.4 eV). To evaluate the robustness of the L-arginine and Ca²⁺ coatings, scratch test was performed to assess their adhesion strength and mechanical stability (Fig. S5). We found the wear rate of the Ca/Arg coatings was 0.00062 mg/(N·m) under a 3 N applied force, indicating that the Arg/Ca²⁺ coatings possessed sufficient adhesion to the SMP substrate and can endure torsional and compressive stresses during implantation [20,21]. This excellent mechanical stability can be attributed to the strong covalent bonding provided by the PDA layer. These findings collectively support the successful PDA, Ca²⁺, and Arg modifications to the SMP-Ca/Arg. Based on the successful implementation in the high Arg loading group, we decided to conduct a more comprehensive exploration into the in vitro osteogenic and angiogenic properties exhibited by the SMP-Ca/Arg2 group.

2.2. The shape memory effect of SMP

A series of tests were performed to assess the shape memory effect of SMP bone screw. As demonstrated in Fig. 2F, the SMP bone screw, initially measuring 2.4 mm in width, could be compressed to 1.8 mm and rapidly recovered its original shape (2.2 mm) upon exposure to warm water at 37°C. This result indicated the SMP bone screw exhibited a robust shape memory effect at physiological temperature. Then, we conducted the compressive tests to determine the mechanical properties of the bone screws, which are critical parameters for resisting torsional deformation during implantation. The PDA/Ca²⁺/Arg coating did not affect the maximum compressive strain (~92%) and the compressive modulus value (~230 MPa) as depicted in Fig. S6. These values indicated that the bone screws possess sufficient stiffness and strength to withstand the mechanical stresses encountered during implantation, ensuring that the screws maintained their shape and functionality under torsional loads. The SMP screw (from 2.4 mm compressed to 1.8 mm) under this compressive modulus generated force from the recovery process, which effectively supported the biomechanical behaviors of the defective sites. The mechanical properties of SMP at 20°C and 37°C were evaluated to analyze their applicability in bone defect sites at room temperature and body temperature. As the temperature transitioned from 20°C to 37°C, the compressive stress (force per unit area developed under compressive loading) of SMP exhibited a slight decrease and did

not significantly affect its mechanical strength (Fig. S7).

Then, repeated compression tests were conducted on SMP bone screws to determine their ability to withstand cyclic fatigue loading conditions. In Fig. 2G, the compressive stress/strain-time curves revealed a gradual increase in compressive stress, rising from 80 MPa to 103 MPa when repeatedly compressing the SMP bone screw with a 50% deformation. Furthermore, cyclic tensile tests were performed, repeated up to ten times (Fig. 2H). In the initial cyclic shape memory test, the fixation ratio and shape recovery rate of the SMP bone screw stood at approximately 89.7% and 91.2%, respectively. This phenomenon is likely attributed to the redistribution and uniform dispersion of hydroxyapatite (HA) particles within the PU matrix during the repeated compressive process. The external mechanical force applied during compression may induce HA particle redistribution with enhanced interaction with the polymer matrix, contributing to improved mechanical properties [22,23]. Additionally, the repeated loading and unloading cycles may also facilitate better alignment and reorganization of polymer chains within the SMP matrix. This reorganization could enhance the material's structural integrity, leading to the observed increase in compressive stress and improved shape memory properties [24,25]. Throughout the subsequent cyclic tests, there was a noticeable improvement in both fixation rate (~95.6%) and shape recovery rate (~99.5%). In addition, the PDA/Ca²⁺/Arg coating did not affect the shape memory effects of SMP bone screws (data not shown).

To assess the mechanical performance of the bone screws during implantation, we firstly performed the finite element analysis (FEA) of the stress situation under torsional forces with a simplified model of the bone defect and SMP screw (Fig. 2J). We found the torsional stress was evenly distributed along the screw threads under forces, ensuring minimal localized stress concentrations that could lead to material failure and provide sufficient resistance to torsional deformation (Fig. 2J). Moreover, our SMP screw showed torsional strength sufficient to withstand the maximum torsional forces applied during surgical insertion without cracking or breaking. Then, we assessed the tight-contacting ability of SMP bone screw after implantation. When the temperature was 20°C, there was no apparent stress in the stress nephograms. As the temperature increased, the recovery stress generated by the bone screws during their return to the original shape became apparent and progressively increased, attributable to the enhanced shape recovery rate of the SMP screw (Fig. S8). At 20°C, no discernible recovery stress was observed in the stress nephograms. However, with rising temperature, recovery stress emerged and subsequently increased as a result of the shape recovery behavior of the SMP screw (Fig. 2I and Fig. S8). Specifically, the SMP screw had nearly 2.219 kPa of the highest von Mises stresses at the interface when the temperature increased to 37°C. The equivalent stress distribution by finite element analysis during the recovery process of the SMP screw in the bone defect site demonstrated that the compressive stress at the interface between the memory screw and the bone was evenly distributed around the periphery of the screw. During mechanical recovery of the SMP, compressive stress generated by the bone screw exhibited a linear recovery trend, which could facilitate defective bone repair through the force stimulation of the bone screw on the surrounding tissues. Furthermore, we chose the commercial metal titanium bone screw and medical bone screw polyetheretherketone (PEEK) as commercial controls to compare the pull-out tests with the SMP screw after implantation into the bone defect site (Fig. 2K). The outcomes indicated that the pull-out force required for the SMP screw significantly exceeded that of the commercial screw, signifying the superior fixation capability of the SMP screw. These results suggest the SMP screw's robust adeptness in suitably fitting bone defects.

2.3. In vitro cell viability, adhesion and proliferation

With the mechanical properties of SMP bone screw properly established, we next evaluated the biocompatibility using rabbit bone

marrow stromal cells (rBMSCs). The survival, adhesion and proliferation of rBMSCs were measured by seeding the cells onto the surface of SMP bone screw following ISO-10993 standard, as these cellular behaviors are closely associated with the bone defect repair process. We found that both SMP exhibited favorable biocompatibility, with cell viability exceeding 90% (Figure S9C-D and Figure S9A). The F-actin/DAPI experiments proved that cSMP material has relatively poor cell adhesion, but the dopamine coating could effectively improve this performance (Fig. S9B). In comparison to the cSMP, the incorporation of Ca²⁺/Arg significantly enhanced the cell adhesion and proliferation capabilities of SMP-Ca/Arg2.

Notably, compared with the cSMP, SMP-PDA and SMP-Ca group, the SMP-Ca/Arg2 group exhibited a significant enhancement in cell adhesion, affirming the advantageous impact of the Arg component on cell adhesion (Fig. S9E) [26]. These findings collectively substantiate the potential of the L-Arginine coated SMP-Ca/Arg2 screws to create a conducive microenvironment for bone defect repair.

2.4. In vitro osteogenesis and angiogenesis

Arg serves as a precursor to NO, while Ca²⁺ regulate NOS activity, activating the NO-cGMP signaling pathway, which promotes osteogenesis and angiogenesis during bone reconstruction [16,17,27,28]. Our engineered SMP-Ca/Arg2 screw could release Arg and Ca²⁺ to active the NOS in rBMSCs and human umbilical vein endothelial cells (HUVECs), and promote generation of NO by catalytical decomposition of Arg. The elevated NO production will trigger the expression of downstream enzyme soluble guanylate cyclase (sGC), cGMP, and protein kinase G (PKG) in the NO-sGC-cGMP-PKG pathway, fostering a coordinated osteogenic-angiogenic effect during bone defect repair (Fig. 3A). The sustained release of Ca²⁺ and Arg from the SMP-Ca/Arg2 bone screw lasted for over 30 days without burst release, which was advantageous for the bone repair process (Fig. 3B and C).

To investigate the signaling pathways in promoting osteogenic and angiogenic differentiation, the effects of SMP-Ca/Arg2 bone screw on osteogenesis and angiogenesis of rBMSCs were evaluated. Alkaline phosphatase (ALP) and alizarin red staining (ARS) analysis were adopted to characterize early and later stage osteogenesis, respectively. As shown in Fig. 3D and E, compared with cSMP group, the osteogenic capabilities of SMP-PDA, SMP-Ca, and SMP-Ca/Arg2 groups were all enhanced, with SMP-Ca and SMP-Ca/Arg2 groups exhibiting better osteogenic performance compared with SMP-PDA on day 3 and 7. In addition, the SMP-Ca/Arg2 group showed a further increase in ALP activity than the SMP-Ca at both time points. The mineral deposition evaluated by ARS analysis showed a similar trend, with the mineral deposition of SMP-Ca/Arg2 group exhibiting the highest ALP activity, indicating optimal in vitro osteogenesis potential (Fig. 3F and G). As the formation of tubular structure by endothelial cells plays a key role in angiogenesis for functional vascular regeneration, we further carried out the tube formation assay to evaluate the angiogenic potential of different SMP materials (Fig. 3H). As the culture time increased, the rBMSCs gradually formed the shape of blood vessels. The SMP-Ca/Arg2 and SMP-Ca group showed better vascularization performance than the SMP-PDA and the cSMP group. The SMP-Ca/Arg2 group could induce the most distinct and vascular-like network structures after incubation with HUVECs for 12 h. Quantitative analysis also demonstrated that the total length and the number of branch points of the formed blood vessels were significantly elevated in the SMP-Ca/Arg2 group with the synergistic effect of Ca²⁺ and Arg (Fig. S10). These results collectively confirmed that the SMP-Ca/Arg2 could promote rapid osteogenesis and angiogenic coupling of rBMSCs and HUVECs.

To confirm the activation of NO-cGMP signaling pathway by releasing ${\rm Ca}^{2+}$ and Arg, the key parameters in the signaling pathway of rBMSCs and HUVECs were evaluated. Tubular structure formed by endothelial cells is a key process in the functional regeneration of blood vessels during angiogenesis. The endothelial NOS (eNOS) is

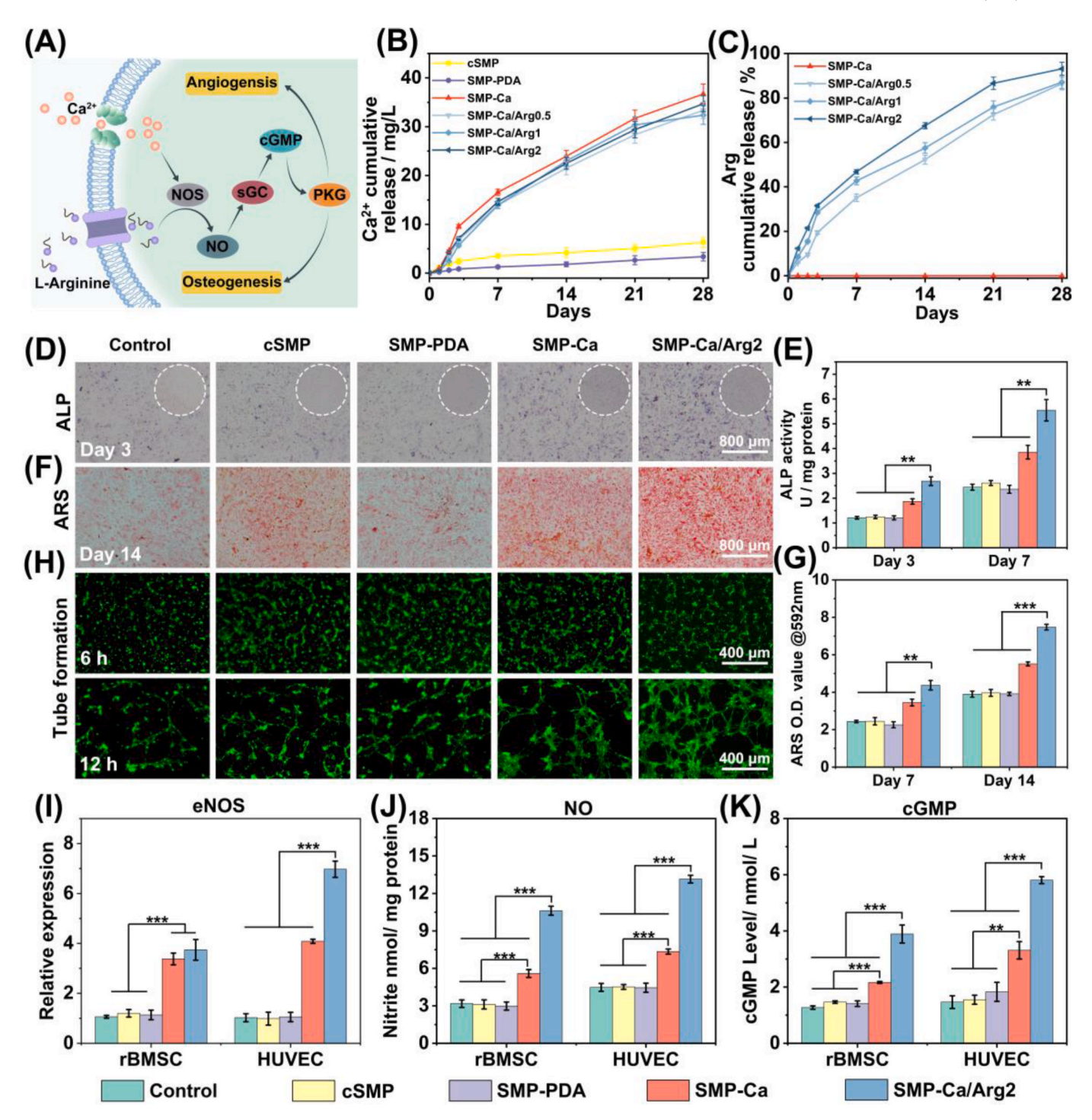


Fig. 3. *In vitro* osteogenesis and angiogenesis potential of SMP bone screw. (A) Schematic illustration showing the released Ca^{2+} and Arg synergistically activate the NO-cGMP pathway, ultimately promoting both osteogenesis and angiogenesis. Release profiles of (B) Ca^{2+} and (C) Arg from different SMP bone screws. (D) Representative ALP staining images (with enlarged images inserted) and (E) quantitative analysis of ALP activity of rBMSCs on day 3 and day 7. (F) Representative ARS images and (G) quantitative analysis of calcium deposition of rBMSCs on day 7 and day 14. (H) Representative fluorescence images showing the endothelial network formation in HUVECs after co-culture for 6 and 12 h. (I-K) Relative expression of angiogenic-related gene expression including eNOS, nitrite levels, and cGMP concentration of rBMSCs and HUVECs on day 3. Data were presented as mean \pm SD and analyzed by one-way ANOVA (n = 3 for each sample, *p < 0.05, **p < 0.01, and ***p < 0.001). These results suggest that Ca^{2+} and Arg synergistically activate the NO-cGMP signaling pathway to promote osteogenesis and angiogenesis.

constitutively expressed in endothelial cells lining the blood vessel, which plays a major role in vascular and tissue protection. eNOS could catalyze the production of NO, a key signaling molecule involved in angiogenesis, from Arg. The expression of eNOS in rBMSCs and HUVECs after co-culturing with different SMP screws for 3 days in Fig. 3I indicated that the SMP-Ca group and the SMP-Ca/Arg2 group presented 2.8-

fold and 3.1-fold increase for rBMSCs and 4.1-fold and 7.1-fold increase for HUVECs, compared to cSMP group. Meanwhile, the level of NO generation and the expression of cGMP, a downstream signaling molecule, for rBMSCs and HUVECs were significantly elevated in the SMPCa/Arg2 group due to the stimulation of NO production by \mbox{Ca}^{2+} and Arg (Fig. 3J and K). \mbox{Ca}^{2+} activated eNOS, catalyzing the decomposition

of Arg within SMP-Ca/Arg2, facilitating NO production. Elevated NO expression further induces the activation of downstream cascades such as sGC, leading to the upregulation of downstream signaling molecules such as cGMP and PKG, consecutively ensuring the continued activation of the NO-cGMP signaling pathway and subsequent coupling osteogenesis-angiogenesis during bone repair. Altogether, the above results demonstrated that the SMP-Ca/Arg2 bone screw could promote

the osteogenesis and angiogenesis through the coordinated activation of NO-cGMP signaling pathway.

2.5. In vivo bone defect repair efficacy

To further examine the therapeutic efficacy of our SMP in bone regeneration, we employed a rabbit femoral defect model to assess both

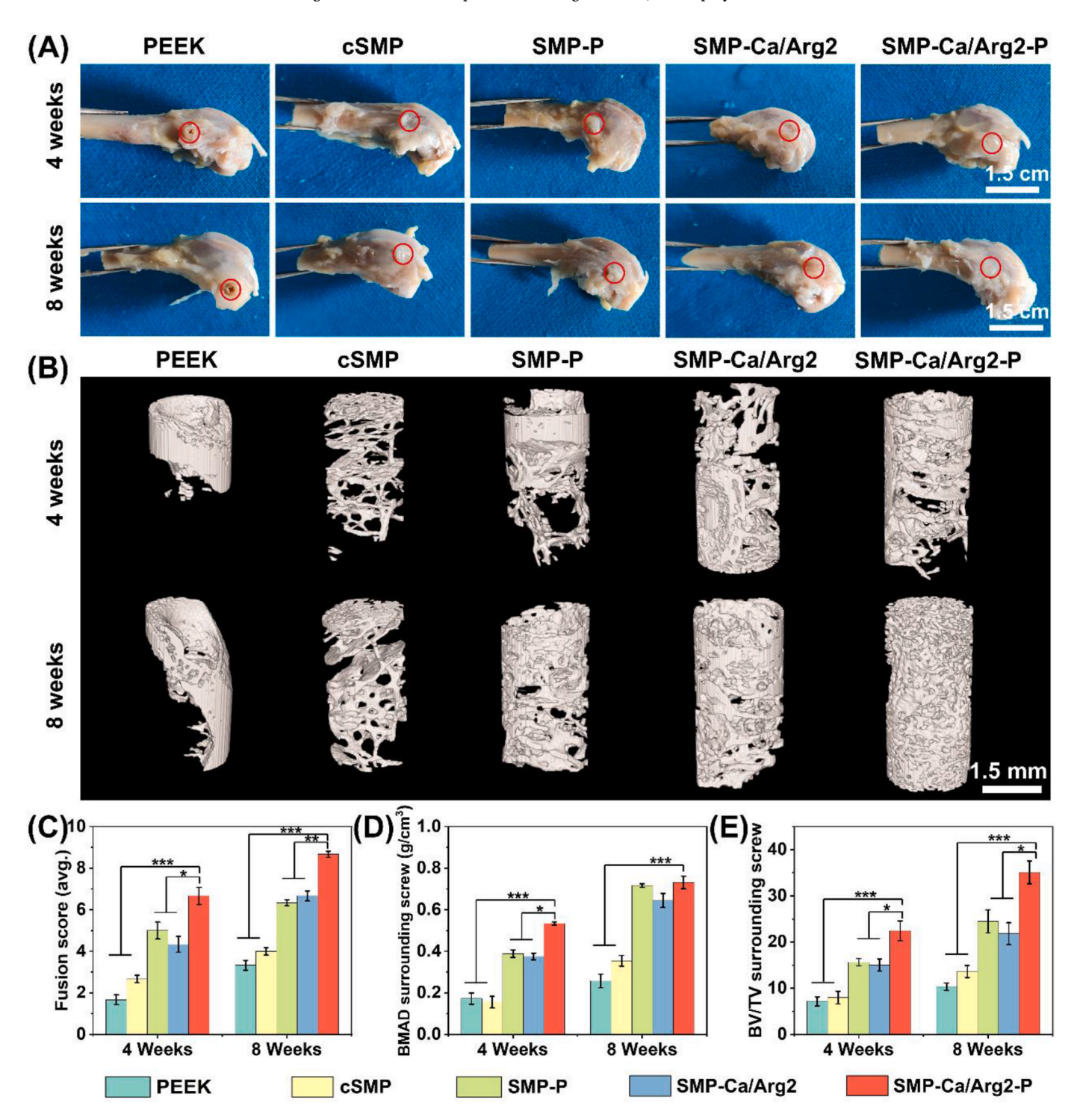


Fig. 4. In vivo bone defect repair efficacy of different SMP screws. (A) Photographs showing rabbit femoral defects after implanting the PEEK screw or SMP screw for 4- and 8- week (the circled regions are the implanting sites); (B) 3D reconstructed micro-CT images of defect areas showing the influences of different bone screws on the new bone formation after implantation for 4- and 8- week. The size of the region of interest (ROI) is ϕ 2.2 mm \times 5 mm; (C) Fusion scores of femoral defects after implanting the PEEK screw or SMP screw for 4- and 8- week; Quantitative statistic of (D) BMAD and (E) BV/TV of the newly formed bone at week 4 and week 8. BMAD: bone mineral apparent density; BV/TV: bone volume/total volume. Data were presented as mean \pm SD and analyzed by one-way ANOVA (n = 6 for each sample, *p < 0.05, **p < 0.01, and ***p < 0.001).

osteogenesis and angiogenesis potential of shape recovery bone screw. Similarly, in total, five groups were tested including: (1) PEEK screw as a clinical control (PEEK), (2) the control naked SMP screw (cSMP), (3) the compressed naked SMP screw (SMP/P), (4) the cSMP screw with optimized Arg and Ca²⁺ coating (SMP-Ca/Arg2), and (5) the compressed SMP-Ca/Arg2 screw, capable of shape recovery and generating recovery stress (SMP-Ca/Arg2-P). Firstly, we extracted rabbit femur samples at 4and 8-week post-surgery following screw implantation (Fig. 4A) and conducted Micro-CT scanning and reconstruction to analyze the formation of new bone (Fig. 4B). Gross observation of rabbit femur after implanting screws were photographed and evaluated according to the adjusted Oswestry Arthroscopy Score (OAS) macroscopic assessment (Fig. 4C). After implantation for 4 weeks, little bone tissue was found around the PEEK screws. Moreover, no significant improvement was found after implantation for 8 weeks. In contrast, bone tissue growth could be observed clearly around the SMP-Ca/Arg2-P bone screw site after implantation for 4 weeks, and the degree of fusion between the SMP-Ca/Arg2-P screw and bone tissue obviously improved overtime. Quantitatively, at each time point, the repair site of the SMP screws had significantly higher scores than that of PEEK screws, indicating much better fusion performances and biocompatibility. It can be easily found that the SMP-Ca/Arg2-P group showed better osteogenesis effect than the cSMP, SMP/P and the SMP-Ca/Arg2 group. At 4- and 8- week postoperation, the new bone formation was analyzed by Micro-CT scanning and reconstruction. Newly formed bone tissues at the defect site could be found in all groups and the SMP-Ca/Arg2-P group showed the maximum amount of dense calcified tissue compared with other groups (PEEK, cSMP, SMP/P, and SMP-Ca/Arg2), indicating the biomechanical and biochemical synergistic effect on promoting osteogenesis (Fig. 4B). For quantitative analysis, the bone mineral apparent density (BMAD) and bone tissue volume/total tissue volume (BV/TV) were calculated (Fig. 4D and E). The BMAD and BV/TV results of the SMP/P and the SMP-Ca/Arg2 group had indicative improvements compared with that of the PEEK group and the SMP group. As for SMP-Ca/Arg2-P group, both the BMAD and BV/TV had a significant enhancement than those in the PEEK and cSMP groups at 4- and 8- week after implantation. For instance, the BMAD and BV/TV of the SMP-Ca/Arg2-P group were 0.74 g/cm³ and 35.2 %, respectively, at 8 weeks, compared to 0.36 g/cm³ and 13.7 % for the cSMP group and 0.26 g/cm³ and 10.4 % for the PEEK group. The SMP-Ca/Arg2-P group demonstrated the maximum new bone formation with highest BMAD and BV/TV values, implying the synergistic influence of Ca²⁺/Arg and the mechanical stress generated by shape memory material on accelerating bone regeneration.

The histological analysis of hematoxylin and eosin (H&E) and Masson's trichrome staining were further carried out to analyze the microscopic detail in the defect site (Fig. 5). The red line in the figure marked means the outline of the uncompressed bone screw, demonstrating that the bone defect was tightly interlocked with bone screw in all groups. No significant enrichment of inflammatory cells was found in all groups. In H&E staining, compared with the PEEK group, more new bone tissues could be found in the SMP groups at each time point due to the better matching of the mechanical properties (Fig. 5A). Moreover, the SMP-Ca/ Arg2-P group had significantly larger area of the new bone tissues after implantation for 4- and 8- week compared to the cSMP screw group, suggesting the synergistic effect of the mechanical stress and the Ca²⁺/ Arg release for osteogenesis promotion. More importantly, significant angiogenesis can be seen in the contact area of bone screw and defect. New vessel density in the SMP-Ca/Arg2-P group (79.02 \pm 7.12 vessels/ mm2) was 116% higher than that in the SMP-P (36.51 \pm 5.91 vessels/ mm²) and 63 % higher than that in the SMP-Ca/Arg2 (48.51 \pm 5.35 vessels/mm²) for 8 weeks (Fig. 5C). Similarly, Masson's trichrome staining also revealed more new bone formation in the SMP-Ca/Arg2-P group (Fig. 5B). It can be clearly interpreted that the SMP-Ca/Arg2-P bone screw effectively promoted the formation of well-organized mature lamellar bone and deposition of collagen fiber in bone defect area. Consistent with the micro-CT results, the histological analysis

presented that the SMP-Ca/Arg2-P group had the highest new bone area fraction (74.71 % \pm 6.35%) compared with the SMP-P (29.25 % \pm 4.51%) and the SMP-Ca/Arg2 (51.06 % \pm 5.47%) group for 8 weeks (Fig. 5D). Histological staining sections also revealed an increase in the number and surface of osteoblasts (Fig. 5E and F) and in the density of viable osteocytes in the defect bone of 4- and 8-week rabbits (Fig. 5G).

Moreover, the screw boundary in the SMP-Ca/Arg2-P and SMP-Ca/Arg2 groups did not completely coincide with the bone ingrowth, likely due to the gradual degradation and release of the bone screw coating and the 0.05 % non-recovery rate of SMP bone screw compression. Biomechanical experiments were further adopted to investigate the effects of the shape memory screws on the compressive strength of the bones. As shown in Fig. S11, at 4- and 8- week after the surgery, the defective bone implanted with coated SMP screws exhibited significantly enhanced mechanical performance, with strength markedly higher than that observed in the cSMP and PEEK groups. This improvement can be attributed to the superior bone repair capacity of the coated SMP screws.

2.6. Mechanism of SMP-ca/arg2-P screw on bone defect repair

As for the SMP-Ca/Arg2-P screw-repaired bone, the stiffness was significantly higher than that of the cSMP screw-repaired bone, providing a good supporting and osseointegration ability to the defective sites. Taken together, the SMP-Ca/Arg2-P could synergistically achieve Arg and Ca $^{2+}$ activated NO-cGMP signaling pathway and compressive stress induced activation of calcium signaling pathway, and finally enhance the formation of new bone and blood vessels.

Finally, transcriptomic analysis of rabbit femoral defect tissue grown on various bone screws were performed to identify the underlying mechanism about how shape memory effect and NO production coating of SMP screw impact bone healing. Principal component analysis generates two separate clusters, indicating that the global gene expression pattern of the SMP-Ca/Arg2-P group exhibited significant difference with the cSMP group as demonstrated by their larger distance between them (Fig. 6A). Consistent with this, the Venn diagram demonstrated a wide range of significant differential gene expressions between the cSMP group and the SMP-Ca/Arg2-P group (Fig. 6B and Fig. S12). Moreover, the SMP-Ca/Arg2-P group presented 22084 total differential expressions genes (DEGs) and 14783 intersecting gene expressions compared with the cSMP group. Specifically, for bone-related genes, the SMP-Ca/Arg2-P group showed extensive differential gene expressions compared to the cSMP group (cSMP vs. SMP-Ca/Arg2-P 1668 genes) with 1222 intersecting genes (Fig. 6B). These results reflected that although both the cSMP bone screw and SMP-Ca/Arg2-P bone screw could promote the bone regeneration, the innate mechanism and the related activation pathways may be vastly different. Additionally, the analysis of DEGs was applied and the volcano plots showed 263 down-regulated DEGs and 1399 up-regulated DEGs in SMP-Ca/Arg2-P group compared with the cSMP group (Fig. 6C).

Then, the Gene Ontology (GO) database evaluation was performed on the DEGs to analyze the functions of DEGs and the role of DEGs in bone regeneration at biological process, cellular component and molecular function level. Compared with the cSMP group, the G protein-coupled receptor signaling pathway, the positive regulation of cell population proliferation, ATP binding, calcium ion binding, and metal ion binding were upregulated in the SMP-Ca/Arg2-P group (Fig. S13). These genes exhibit a close association with translation, signal transduction, cell differentiation, cell adhesion, and intracellular signal transduction, and they play an integral role in the intricate process of new bone formation.

In addition, Kyoto Encyclopedia of Genes and Genomes (KEGG) pathway enrichment analysis of the DEGs was further performed to reveal the functions of DEGs. Compared to the cSMP group, the results indicated calcium signaling pathway, PI3K-Akt and cGMP-PKG signaling pathway related to osteogenesis and angiogenesis were

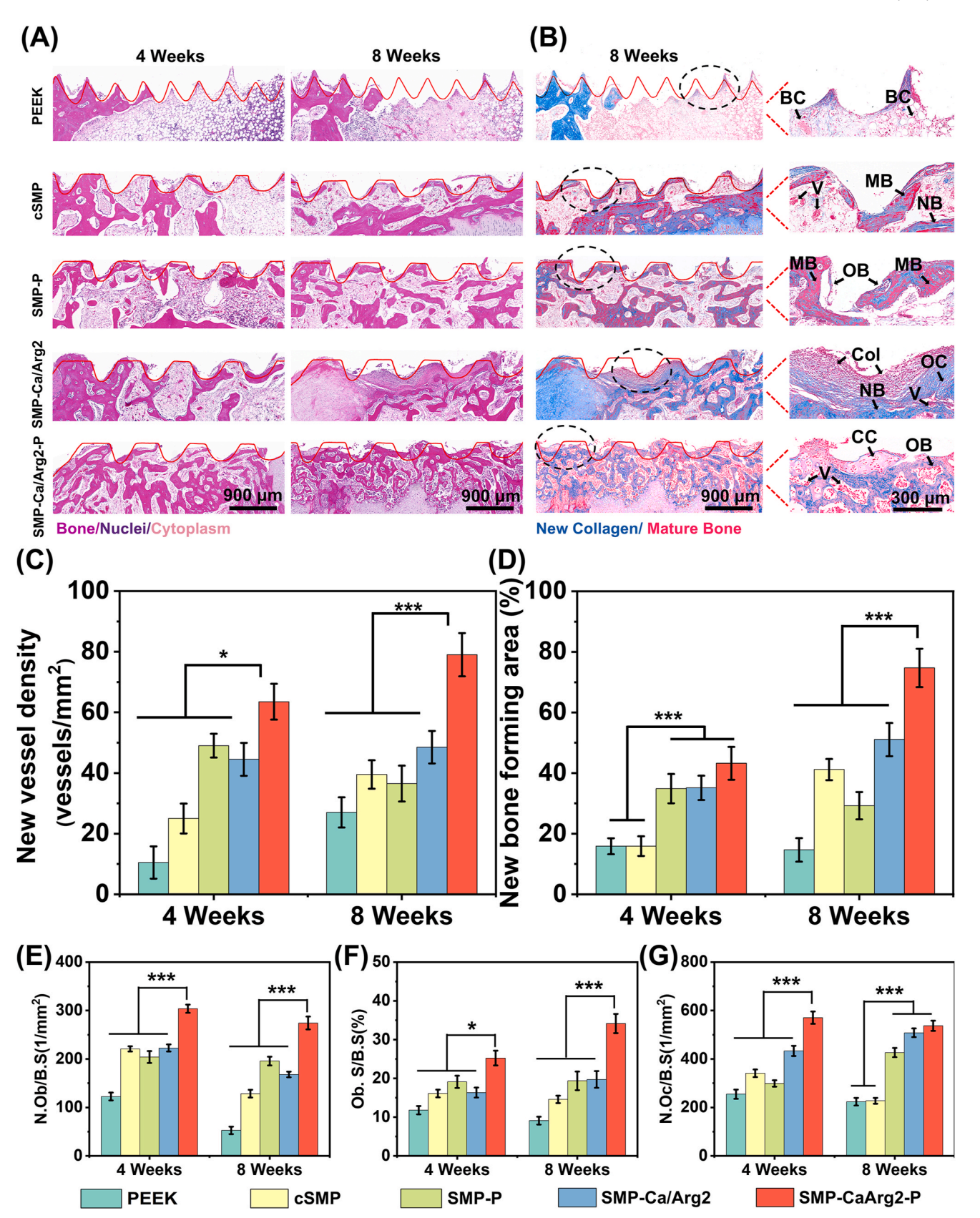


Fig. 5. Histological investigation of the bone screws. (A) Tissue sections of the defective site with the screws after implantation for 4 and 8 weeks stained with H&E; (B) Tissue sections and magnified views of the defective site with the screws after implantation for 8 weeks stained with Masson. Red curve: the outline edge of SMP screw. NB: new bone; MB: mature bone; OB: osteoblast; OC: osteocyte; BC: blood cell; V: vessel; CC: chondrocyte; Col: collagenous tissue. (C) New blood vessel density. (D) Percentage of new bone area. (E) Osteoblast number per bone surface (N.Ob/B.S), (F) Osteoblast surface per bone surface (Ob.S/B.S) and (G) Osteocyte number per bone surface (N.Oc/B.S) after implantation 4- and 8- week rabbit femoral defect model. Data were presented as mean \pm SD and analyzed by one-way ANOVA (n = 6 for each sample, *p < 0.05, **p < 0.01, and ***p < 0.001).

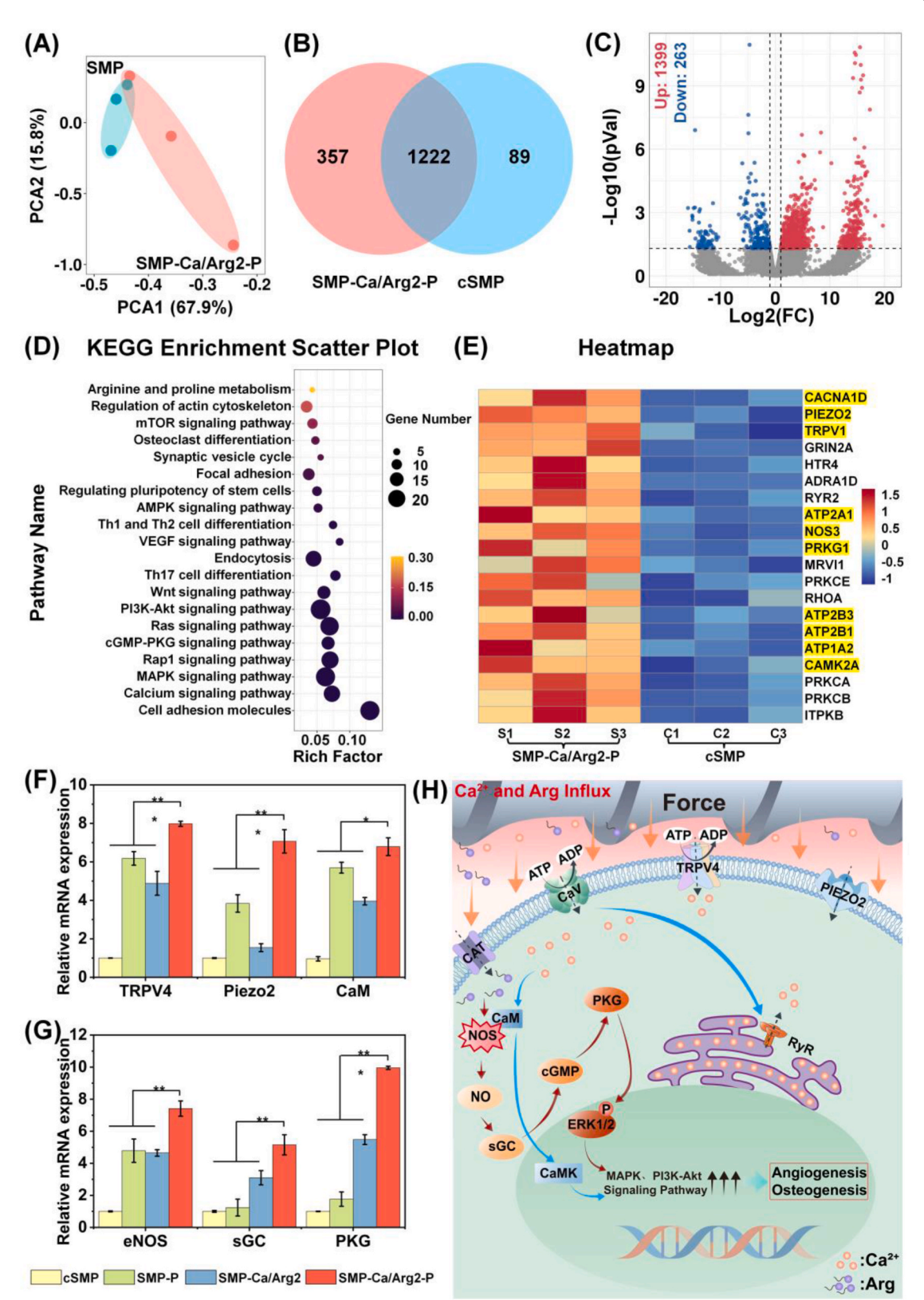


Fig. 6. Bioinformatic analysis of gene expression of rMSCs on different bone screws. (A) Principal component analysis of gene expression profile of rMSCs grown in the presence of cSMP screw or SMP-Ca/Arg2-P screw; (B) Venn diagram illustration of the significant DEGs between the SMP-Ca/Arg2-P group and the cSMP group; (C) Volcano plots of transcriptomic analysis of DEGs in cSMP versus SMP-Ca/Arg2-P; (D) Up-regulated enriched Kyoto Encyclopedia of Genes and Genomes pathways of cSMP versus SMP-Ca/Arg2-P; (E) Heatmap evaluation of up-regulated DEGs involved in mechanosensitive calcium, PI3K-Akt and cGMP-PKG signaling pathways; (F-G) Relative messenger RNA expression evaluation of targeted genes via qRT-PCR; (H) Schematic illustration of potential SMP-Ca/Arg2-P-mediated activation of the mechanosensitive and NO-cGMP signaling pathway for coupling osteogenesis-angiogenesis. Sample size n=3 for all experiments. Data were presented as mean \pm SD and analyzed by one-way ANOVA (n=6 for each sample, p<0.05, p<0.01, and p<0.001.

significantly enriched in the SMP-Ca/Arg2-P group (Fig. 6D). The above GO and KEGG results matched well with the bone defect repair efficacy and the histomorphological results (Figs. 4 and 5). The bone regeneration process started with the formation of mature lamellar bone and deposition of collagen fiber in the defect sites in the SMP-Ca/Arg2-P group, and the cell surface, cell chemokine, absorption, metabolism, osteogenesis, and angiogenesis related GO terms and KEGG pathways were all enriched. Therefore, the main function of the SMP-Ca/Arg2-P bone screw to promote bone defect repair was embodied in the development and regeneration, metabolism, and signal transduction.

Furthermore, the heatmap analysis was performed on the DEGs between the SMP-Ca/Arg2-P group and the cSMP group (Fig. 6E). The genes were selected based on GO and KEGG pathway enrichment analyses, specifically focusing on pathways associated with mechanosensitive signaling, calcium signaling pathway, metabolism, and osteogenesis and angiogenesis pathways. Consequently, we identified a series of genes (e.g., TRPV1, PIEZO2, CACNA1D, CaM, ATP1A2, ATP2A1, RyR, NOS3, and CaMK) that were significantly upregulated in the SMP-Ca/ Arg2-P group. These genes indicated that the implantation of SMP-Ca/ Arg2-P screws was not only associated with the activation of osteogenesis and angiogenesis related signaling pathways but also played a pivotal role in modulating cellular metabolism toward tissue regeneration. To confirm the RNA sequencing results, we performed qRT-PCR experiments with a subset of genes most closely related to the mechanosensitive calcium channel signaling pathway and the NO-cGMP signaling pathway, which were critical for understanding how biomechanical and biochemical cues synergistically regulated osteogenesis and angiogenesis. Specifically, we selected genes that serve as key indicators of these pathways, including TRPV4 (transient receptor potential vanilloid 4), PIEZO2 (Piezo-type mechanosensitive ion channel component 2), and CaM (calmodulin) from the mechanosensitive calcium channel signaling pathway, and eNOS (endothelial nitric oxide synthase), sGC (soluble guanylate cyclase), and PKG (protein kinase G) from the NO-cGMP signaling pathway. The qRT-PCR results showed that the expression of these genes in the SMP-Ca/Arg2-P group was markedly higher than in the cSMP, SMP/P, and SMP-Ca/Arg2 groups, which were consistent with the RNA sequencing results (Fig. 6F and G). To further validate our findings, we performed Western blot (WB) analyses to assess the expression levels of key proteins involved in these pathways (Fig. S14). The WB results demonstrated excellent consistency with the qRT-PCR data, confirming that the upregulation observed at the transcriptional level was also reflected at the translational level. This validation reinforced our conclusion that the SMP-Ca/Arg2-P group effectively activated mechanosensitive calcium channel and NO-cGMP signaling pathways, thus promoting osteogenesis and angiogenesis.

In our study, the SMP-Ca/Arg2-P bone screw released Ca²⁺ and Arg while concurrently exerting mechanical forces for activation of mechanosensitive pathways through the shape memory effect, leading to synergistical facilitation of bone tissue regeneration. The mechanosensitive ion channels on the surface of cell membrane represent a family of proteins that can act as both effectors and sensors. They can translate the mechanical forces that are applied onto the cellular signals to impact bone metabolism [29]. The compressive force exerted by shape memory effect of SMP could activate mechanosensitive calcium signaling pathway (e.g., TRPV4, PIEZO2, and CaV) and promote the inward flow of Ca²⁺. Meanwhile, the CaV membrane channel protein directly upregulates the ryanodine receptor (RyR) protein, leading to the efflux of Ca²⁺ into the cytoplasm. Therefore, this leads to a continued rise in Ca²⁺, stimulating the production of CaM protein and activation of the NO-cGMP pathway, expediting the cellular ATP synthesis. ATP, through phosphorylation, can regulate multiple ion channels and transporters when the extracellular ATP concentration increases. An elevation in extracellular ATP concentration prompts its binding to TRPV4 and CaV channel proteins, resulting in their activation and subsequent Ca²⁺ influx, triggering a positive feedback loop that further promotes the production of CaM protein. Meanwhile, the membrane

protein cationic amino acid transporter (CAT) facilitates the influx of Arg by utilizing the released Arg from the SMP-Ca/Arg2-P. The cooperation of Arg influx and upregulation of CaM enhances the expression of the NOS protein, resulting in the production of NO. This also triggers the NO-cGMP pathway, activating downstream enzymes such as sGC, cGMP, and PKG. Furthermore, Arg has been confirmed to reverse the TNF- α -induced blockade of oxidative phosphorylation, leading to a reduction in osteoclastogenesis [30]. Arg is converted into 2-oxoglutarate (also known as α -ketoglutarate), acting as a precursor for glucose, and then directly participates in the energy metabolism through oxidative phosphorylation. The supplementation of Arg could significantly decrease glucose consumption, while the level of glycolysis and ATP production remain stable. Consequently, ERK1/2 in the nucleus is regulated, facilitating angiogenic functions.

Concurrently, the Ca²⁺ influx induced by the mechanical force can modulate osteogenesis by activation of related osteogenic channels (e.g. Calcium signaling pathway, PI3K/Akt and cGMP-PKG signal pathway). It is considered that this is the first instance of functionalizing bone transplant materials to activate mechanosensitive and NO-cGMP pathways, enabling them to provide robust support while synergistically enhancing osteogenesis, angiogenesis, and regulation of cellular metabolic processes.

These processes also impact cellular metabolic activities, for instance, by promoting the generation of ATP through the activation of AMPK and PI3K/Akt signaling pathway. PI3K/Akt pathway plays a major role in regulating the cellular uptake of glucose and membrane synthesis. The activated PI3K/Akt could promote lipid synthesis from glucose carbon by multiple mechanisms, increase the overall glycolytic rate in the cell, enhance ATP consumption, and coordinate cellular growth and division [31]. Meanwhile, the AMPK and mTOR signaling are key regulator of cellular metabolism, both of which play key roles in cell proliferation, growth regulation and metabolism reprogramming [32,33]. Upon activation of AMPK, catabolism is enhanced to provide more energy, and anabolism is slowed down to avoid overdraft of the ATP. Therefore, cells maintain energy homeostasis with the assistance of the glucose and energy sensor AMPK, which is essential for cell proliferation and cellular metabolism. Altogether, these studies indicate that the SMP-Ca/Arg2-P bone screws not only activate the NO-cGMP pathway through the synergistic effects of Ca²⁺/Arg release and mechanical force stimulation, but also regulate cellular metabolism. This enhanced the cellular glycolytic rate, regulated cell proliferation and differentiation, and ultimately promoted bone tissue regeneration. This study, for the first time, elucidated the synergistic regulatory mechanism of mechanical forces and Arg/Ca²⁺ in osteogenesis and angiogenesis for bone regeneration. It demonstrated that this process was dependent on cellular metabolism regulation, affecting cell proliferation and differentiation, and promoting bone tissue regeneration. This mechanism has significant implications for the therapeutic use of mechanical force-signaling pathways and cellular metabolism in treating bone fractures and osteoporosis.

3. Conclusions

In the present study, a programmable bone screw fabricated by PU, HA, Arg and ${\rm Ca}^{2+}$ with strong internal fixation and effective repair ability has been developed for bone regeneration. The SMP bone screw exhibit outstanding mechanical properties and shape memory performance with a compressive modulus of approximately 230 MPa, and fixation ratio and shape recovery rate close to 95.6 % and 99.5 %. Consequently, the SMP bone screw can be easily compressed at $60^{\circ}{\rm C}$ into a smaller size for minimally invasive implantation, and subsequently expand at $37^{\circ}{\rm C}$ to exert stress on the surrounding tissues (approximately 80 MPa). The *in vivo* and *in vitro* experiments demonstrate that SMP-Ca/Arg2 bone screw shows good biocompatibility and does not appear to elicit inflammatory responses. The SMP-Ca/Arg2 bone screw can long-term release Arg and ${\rm Ca}^{2+}$ to active the NO-

cGMP signaling pathway and promote bone tissue formation. Moreover, the mechanical force released by the shape memory process of SMP-Ca/ Arg2-P bone screw can activate the mechanosensitive calcium ion channel (e.g., TRPV4, PIEZO2, CaM, and CAT), promoting the inward flow of Ca²⁺ and further switch on the NO-cGMP pathway. The synergistic effect of mechanical force and Arg/Ca²⁺ could accelerate bone healing by osteogenesis-angiogenesis coupling to promote bone and vascular regeneration. This study is the first to propose that mechanical force-induced Ca²⁺ influx, along with Arg/Ca²⁺ release, can activate mechanosensitive and NO-cGMP signaling pathways, thereby achieving coordinated regulation of osteogenesis and angiogenesis during bone regeneration. We demonstrate that this process is dependent on cellular metabolic regulation, ultimately affecting cell proliferation and promoting osteogenesis. This theoretical mechanism has significant implications for the application of mechanotransduction-signaling pathwayscell metabolism in disease treatment, e.g., bone fracture and osteoporosis. Considering the noteworthy advantages of SMP-Ca/Arg2-P bone screw including shape memory effect, cytocompatibility, fixation and osteogenic and angiogenic properties, we believe that the shape memory composite bone screw could provide a novel treatment with enhanced efficacy in repairing bone defects.

4. Methodology

4.1. Design, fabrication, and characterization of SMP materials

4.1.1. Synthesis of SMP materials

The synthesis process of SMP materials has been discussed in our previous work [19]. In brief, a mixture of the dried polycaprolactone diol (PCL-diol) 10 mmol (Mn: 530, Sigma-Aldrich) and methylene diphenyl diisocyanate (MDI) 42 mmol (Mw: 250.25, Sigma-Aldrich) were poured into a 150 mL flask and reacted at 85 °C for 2 h with mechanical stirring at 200 rpm under nitrogen protection to synthesize the PU prepolymer. Then, 2.4 wt% HA (Mw: 1004.62 g/mol, Sigma-Aldrich) was dispersed in the above flask with mechanical stirring at 200 rpm for 1 h followed by removal of oxygen at 85 °C under vacuum for 1 h. Purified 1,4 Butanediol (BDO) 30 mmol (Mw: 90.12 g/mol, Sigma-Aldrich) was then added and mechanically agitated for 40 s at 1000 rpm to polymerize the mixture, and the resultant mixture was gently poured onto a glass slide, respectively, to manufacture SMP film (Fig. S15).

Subsequently, we designed the size of SMP screw following the modified intercondylar fractured rabbit model as shown in Fig. S16. An appropriate silicone screw mold was manufactured using this design as a template to hold the fabricated SMP bone screws, which were produced through hot press molding, and underwent a sequential coating process as specifically described below. The hot press molding process used to fabricate the SMP bone screws involved heating to $85^{\circ}\mathrm{C}$ for $30~\mathrm{s}$ to achieve the initial curing and shaping. However, to ensure the required mechanical strength, the SMP bone screws were subsequently maintained at $85^{\circ}\mathrm{C}$ for 24 h, allowing for complete curing and optimal mechanical properties.

4.1.2. Ca²⁺ and Arg coating on PU/HA substrate

The PU/HA (SMP base material) film (size: $10\times50\times1$ mm) and screw substrate were used to conduct the surface modification. The SMP base materials were immersed in a 2 mg/mL of dopamine-Tris-HCL solution (pH: 8.0) for 24 h to form a uniform, dense and adhesive PDA layer and named as SMP-PDA. The samples were washed with 50 mL of ultrapure water three times, and then allowed to dry in air. Then, SMP-Ca materials were fabricated by coating in a solution containing CaCl₂ (2 mg/mL) for 24 h utilizing the adhesion effect of polydopamine. Final SMP-Ca/ArgX samples were fabricated by a subsequent coating in a solution containing CaCl₂ (2 mg/mL) and Arg (X mg/mL, X = 0.5, 1, and 2) for 24 h utilizing the adhesion effect of polydopamine, thoroughly rinsed with ultrapure water as indicated above, and dried under vacuum for 24 h.

4.2. Characterization of SMP and its composite

The Fourier transform infrared (FTIR) spectra were recorded to validate the synthesized SMP materials and the PDA, ${\rm Ca^{2^+}}$, and Arg coating by using an attenuated total reflectance Thermo Scientific Nicolet iS2 spectrometer [34,35]. The Raman spectra were adopted to evaluate the chemical structures of the synthesized SMP and its coatings by using a Renishaw Micro-Raman Spectroscopy System with a 785 nm laser excitation wavelength in a wavenumber range of $100-3200~{\rm cm^{-1}}$. An X-ray photoelectron spectroscopy spectrometer (XPS, Thermo Fisher Nexsa) was employed to evaluate the elemental compositions of SMP materials (sample size: $5 \times 5 \times 1~{\rm mm}$) [36]. A goniometer (OCA-20) was applied to measure the water contact angle of SMP samples to determine the surface wettability of the materials [36]. The general surface morphologies of SMP films and screws could be observed by scanning electron microscopy (SEM, Tescan VEGA3).

The shape memory effects of the SMP materials were evaluated in the form of the block samples (size: $10 \times 10 \times 10$ mm) and the screw samples using an INSTRON 5566 universal testing machine. The cyclic compression was performed at 60°C with a compressive rate of 1.0 mm/ min. The screw cap was removed for even stress before testing, and the SMP block and screw samples were positioned horizontally before compression. The samples were fixed and relaxed through the clamps and the shape memory effect was carried out as follows [12,37,38]. The compressive process of the SMP samples was performed systematically to achieve circumferential deformation. Specifically, the steps were as follows: (a) Fixing and heating: The SMP screw samples were securely held in place using clamps to ensure uniform stress distribution. The samples were then heated to 60°C for 10 min to eliminate any potential thermal phase transition and ensure the material was in a pliable state for deformation. (b) Compression: The screws were compressed circumferentially to 50% deformation (ϵ_m) under 60°C using a custom-designed setup. This was achieved by applying radial compressive force that uniformly reduced the diameter of the screw while maintaining its axial alignment. (c) Cooling to lock the temporary shape: While maintaining the compressed state at ε_m , the samples were cooled down to 25°C for 10 min. This cooling step allowed the shape memory polyurethane (PU) to lock into its temporary compressed configuration, making the screw slimmer. (d) Releasing the Clamps: After cooling, the clamps were released ($\sigma = 0$), and the strain of the sample in its temporarily compressed shape was recorded as ε_{u} . (e) Shape Recovery: To evaluate the shape memory effect, the compressed samples were heated to 37°C (body temperature) and maintained for 10 min. During this step, the screws reverted to their original shape due to the activation of the shape memory effect, and the recovered strain was recorded as $\varepsilon_{\rm m}$. The procedures were repeated 10 times to generate the thermal cyclic compressive curves. The shape fixation rate (Rf) and shape recovery ratio (Rr) represented the performance of the final fixed deformation and the ability to memorize the original size of a sample, respectively. Therefore, Rf and Rr, as the most two important parameters for investigating the ability of shape memory properties, were calculated by using the following Equations (1) and (2) with the above strain and stress data [12].

$$Rf(N) = \frac{\varepsilon_u(N)}{\varepsilon_m} \times 100\%$$
 (1)

$$Rr(N) = \frac{\varepsilon_m - \varepsilon_p(N)}{\varepsilon_m - \varepsilon_p(N-1)} \times 100\%$$
 (2)

where N stands for the repeat times ($N \ge 1$).

4.3. Mechanical and shape memory properties of SMP

The pull-out experiments were conducted employing the INSTRON 5566 universal testing machine for evaluating the fixation performance $\frac{1}{2}$

of the SMP samples [13,34]. To simulate minimally invasive surgery that involves implanting bone screws, the SMP samples were programmed as a smaller temporary shape (diameter: 1.8 mm) and implanted into the bone defect (diameter: 2.0 mm) in a PU foam [39]. The screw pull-out experiment was conducted. Initially, the bone screw was compressed to 50% deformation at 60° C, and then cooled to 25° C and fixed for 10min by using the clamp. The screw was then implanted into the defect of the model, and the clamp was removed. Next, the bone screw was heated at 37°C for 10 min to trigger shape memory recovery, followed by cooling to room temperature for an additional 10 min. Subsequently, a clamp was used to secure the screw cap, and the screw was subjected to axial tensile testing at a rate of 1 mm/min, parallel to the direction of insertion. The extraction forces were measured and compared for the SMP, PEEK, and titanium metal screws to evaluate their fixation performance and the stability of the bone-screw interface. For the scratch test, the friction stroke was set to 3 mm, with a total friction time of 120 min. This corresponded to repeatedly applying a 3N force over the same area of the coating, simulating the mechanical stresses experienced during implantation. The wear rate was then calculated by measuring the mass loss of the coating under these condition.

4.4. In vitro release of Arg and Ca²⁺

The SMP-Ca/Arg0.5, SMP-Ca/Arg1, and SMP-Ca/Arg2 screws were placed into 2 mL of Ca²⁺/Mg²⁺-free phosphate-buffered saline (PBS) solution and incubated for 4 weeks to measure the Arg and Ca²⁺ release profiles [40]. At predetermined time points, 50 μL of solution was collected for analysis, while the same volume of fresh PBS was supplemented to continue the experiment. The releasing dosage of Ca²⁺ was calculated using the collected solution by inductively coupled plasma mass spectrometry (ICP-MS) Agilent 7700 [17]. For testing the property of SMP-Ca/Arg screw in releasing Arg, the total loading dosage of SMP-Ca/Arg0.5, SMP-Ca/Arg1, and SMP-Ca/Arg2 were determined using an Agilent 1260 Infinity II high performance liquid chromatography system, operating with the openlab CDS acquisition. For testing the property of SMP-Ca/Arg screw in releasing Arg, the total loading dosage of SMP-Ca/Arg0.5, SMP-Ca/Arg1, and SMP-Ca/Arg2 were determined using an Agilent 1260 Infinity II high performance liquid chromatography (HPLC) system, operating with the openlab CDS acquisition. The bone screws were firstly immersed in 2 mL of an Arg solution (X mg/mL, X = 0.5, 1, and 2) for 24 h. After that, the screw was rinsed with 2 mL of ultrapure water for three times. The washing solution and the soaking solution were combined, and 5 μ L of the mixed solution was analyzed using HPLC. The chromatographic separation was performed using an Agilent TC-C18 column with dimensions of 4.6 \times $250\ mm$ and a particle size of 5 $\mu m.$ The mobile phase consisted of acetonitrile and a 0.02 mol potassium dihydrogen phosphate solution (with phosphoric acid to adjust the pH value to 3.0) in a ratio of 70:30. The flow rate was set at 1.0 mL/min, and the column temperature was maintained at 30 °C. A sample injection volume of 5 μL was used, and the detection wavelength was set at 206 nm. The loading amount of Arg was then determined by comparing the initial concentration and volume with the residual concentration following Equation (3). To ensure the accuracy of the findings, each independent Arg release test was conducted at least three times, and the results were expressed as the mean

 \pm standard deviation for eliminating experimental error.

Drug release percentage =
$$\frac{\text{amount of release SMP}}{\text{total amount of loaded SMP}} \times 100\%$$
 (3)

4.5. In vitro biocompatibility characterization

Rabbit bone marrow stromal cells (rBMSCs, Cyagen, Hong Kong) were selected to investigate cell viability, adhesion, and proliferation of the SMP materials. Five groups, including control (PBS), cSMP (control

naked PU/HA material), SMP-PDA (shape memory PU/HA materials with PDA coating), SMP-Ca (shape memory PU/HA materials with Ca²⁺ by PDA adhesion), SMP-Ca/Arg2 (shape memory PU/HA materials with Ca²⁺ and Arg by PDA adhesion) were involved in the test. The biocompatibility experiments were conducted by using rBMSCs with α-Minimum Essential Medium (α-MEM, Gibco, Hong Kong) supplemented with 10 % (v/v) fetal bovine serum (FBS, Gibco, Hong Kong) and 1 % (v/v) Penicillin-Streptomycin (P/S, Gibco, Hong Kong) in the incubator following the standard of ISO-10993. Briefly, all samples were cut into small pieces (size: 10 mm \times 50 mm \times 0.5 mm). Before cell seeding, the samples were sanitized and placed in 4 mL of culture media for 24 h. After that, the extraction solutions were applied into the plate wells for further investigation. The rBMSCs were seeded using the extracted tissue culture media at 1×10^4 cells/cm² and incubated for 3 days. The Live/Dead assay kit (Thermo Fisher) and PicoGreen assay kit (Thermo Fisher) were adopted at pre-determined time points [41]. The cell viability and morphological images were captured using the Nikon ECLIPSE Ts2R microscope, while the quantitative assessment of cell viability and proliferation was performed using the SYNERGY HTX multi-mode reader. Furthermore, cell adhesion and morphology were conducted on the surface of the samples at 1×10^4 cells/cm⁻² after incubating for 3 days using a Leica TCS SPE confocal microscope. The quantitative data of the cell spreading area for investigating cell adhesion performance was analyzed by using Fiji Image J software [42].

4.6. Osteogenic differentiation and angiogenesis paracrine potential assessment

4.6.1. Osteogenic differentiation potential of SMP materials

The effect of SMP on rBMSCs osteogenesis was evaluated based on a co-culture system. Briefly, 2×10^4 cells/cm² rBMSCs were seeded on the surface of a variety of SMP substrates (size: $10 \text{ mm} \times 10 \text{ mm} \times 0.5 \text{ mm}$) in 1 mL osteogenic medium (Cyagen, China). On day 3 and 7, the ALP activity was measured using an ALP quantification kit (Beyotime, China). After 7 and 14 days of incubation, using the manufacturer's provided protocol of ARS staining kit (Solarbio, China), the generation of mineralized matrix on the SMP materials was further assessed [43].

4.6.2. Angiogenesis paracrine potential of SMP materials

Similarly, the effect of the prepared SMP samples on angiogenesis of human umbilical vein endothelial cells (HUVECs, Cyagen, Hong Kong) was evaluated based on ISO 10993 standard. In brief, HUVECs were seeded onto a 24-well plate coated with Matrigel at a density of 5×10^4 cells/cm² using 1 mL extracted SMP material tissue culture medium as used in the cell viability assay. After 6 and 12 h, the HUVECs were stained with Calcein AM (Thermo Fisher, China), and the images were captured using a Nikon ECLIPSE Ts2R microscope. Subsequently, the total length and average number of branching points were analyzed using Fiji Image J software.

4.6.3. Mechanism study of SMP on angiogenesis

Arg and Ca^{2+} affect NO production by regulating the expression of proteins in the NO-cGMP signaling pathway. To assess the expression of significant signaling protein in the NO-cGMP signaling pathway, the eNOS level was measured by enzyme-linked immunosorbent assay (ELISA) and the NO production was quantified employing the total NO kit (Beyotime, China). Briefly, the rBMSCs/HUVECs were seeded at 5 \times 10⁴ cells/cm² on a variety of SMP samples cultured in the medium. The nitrite content in the culture supernatants of the rBMSCs/HUVECs was determined after 3 days of incubation using total NO assay kit [44]. By using the Griess technique to measure the concentration of nitrite, the NO production was investigated [45]. Similarly, on day 3, the cGMP ELISA kit (Bioss, China) was used to measure the amount of cGMP.

4.7. In vivo bone regeneration assessment

We performed the rabbit femoral defect model to assess the therapeutic efficacy of bone regeneration of the SMP bone screws [46]. All animal evaluation was performed with approval from the Ethics Committee of the Affiliated Suzhou Hospital of Nanjing Medical University (K-2023-044). A total of 60 New Zealand white rabbits (male, 2.5–3 kg) were adopted and randomly divided into five groups and two times (4 weeks and 8 weeks), PEEK (positive control), cSMP, SMP/P, SMP-Ca/Arg2, and SMP-Ca/Arg2-P (n = 6 per group for each time point). This is because the acceptable range of degree of freedom (DF) was between 10 and 20 and n = 6 could satisfy the power analysis [47]. We then anesthetized the rabbits with pentobarbital sodium and created a 6-cm skin incision to expose the femoral condyle. Next, a dental drill was used to create a 2.0 mm diameter round defect on the exposed femoral condyle. We then implanted the PEEK and programmed SMP screws (size: 10 mm \times ϕ 1.8 mm) and sutured the defect sites of the rabbits. After 4- and 8- week post-operation, the rabbits were sacrificed with CO₂ suffocation and the femur samples were harvested. The high-resolution micro-CT (SkyScan 1176, Belgium) was applied to quantify the bone repair [48]. The different thresholding ranges (threshold for new bone = $80 \sim 140$, screw = 140) were applied to distinguish the new bone and the screw [49,50]. The ROI was selected around the bone defect where the screw was located (size: $\phi 2.2 \text{ mm} \times 5$ mm), and quantification results such as bone density and volume within this ROI were calculated by the CTAn software (Bruker, Belgium). The 3D images were reconstructed by the NRecon software (Bruker, Belgium). Then, the biomechanical behaviors were evaluated by the INSTRON 5566 universal testing machine to evaluate bone regeneration performance. Briefly, the upper and lower surfaces of the femur were in complete contact with the fixtures. A preload of 10 N was applied, followed by a loading rate of 2 N/s. The test was terminated upon failure of the samples. The testing machine continuously recorded the load-displacement changes and the stiffness among different groups was compared. Furthermore, the femur tissue sample was fixed and processed, and then embedded and sectioned using an AICA300 hard tissue slicer. Subsequently, H&E and Masson staining were conducted to investigate the formation of new bone tissues in the defect sites. The gene sequence analysis of the femur samples was performed to analyze the bone regeneration coupling effect and the potential downstream signal pathways activated in the regeneration sites. The NEBNext® Ultra™ RNA Library Prep Kit was used to create the RNA-Seq libraries [36]. The Illumina HiseqX-ten platform sequenced the pooled library. Then, we performed the qRT-PCR to analyze the osteogenic gene expression (TRPV4, PIEZO2, CaM, Enos, sGC, and PKG) [51]. Briefly, total RNA was isolated from rabbit femoral defect tissue implanted with PEEK and SMP screws using trizol reagent (Genstar, China). We performed qRT-PCR after utilizing reverse transcription to generate cDNA with the CFX 96 detection system (Bio-Rad, USA). Primers of target genes were listed in Table 1 (support information). Western blot (WB) analysis was performed to validate the protein expression levels of key genes identified through RNA sequencing and qRT-PCR. Total protein was extracted from samples using RIPA lysis buffer supplemented with protease and phosphatase inhibitors. Protein concentrations were measured using a BCA protein assay kit. Equal amounts of protein (20 ug) were separated via SDS-PAGE and transferred onto PVDF membranes. The membranes were then blocked with 5 % non-fat milk and incubated with primary antibodies overnight at 4 °C, followed by incubation with HRP-conjugated secondary antibodies. Protein bands were visualized using an enhanced chemiluminescence (ECL) detection.

4.8. Statistical analysis

Each test was conducted four times unless otherwise stated, and the results were provided as mean \pm standard deviation. GraphPad Prism Software (GraphPad Software Inc.) was used to investigate statistical

comparisons between each group using one-way ANOVA with Tukey post-hoc. Statistical significance was defined as a difference at *p < 0.05, **p < 0.01, or ***p < 0.001.

CRediT authorship contribution statement

Huaqian Liu: Writing – review & editing, Writing – original draft, Visualization, Validation, Methodology, Investigation, Formal analysis, Data curation, Conceptualization. Weiwei Zhao: Writing – original draft. Yuhe Yang: Writing – review & editing, Conceptualization. Ho-Pan Bei: Writing – review & editing. Qunchao Chen: Investigation. Xintong Zhou: Investigation. Yuanchi Zhang: Conceptualization. Chunyi Wen: Conceptualization. Yuefeng Hao: Conceptualization. Jinlian Hu: Conceptualization. Yaxiong Liu: Conceptualization. Yu Zhang: Conceptualization. Ka-Hing Wong: Conceptualization. Hongyu Zhang: Writing – review & editing, Writing – original draft, Visualization, Funding acquisition, Conceptualization, Supervision, Resources, Project administration, Investigation, Funding acquisition, Conceptualization.

Ethics approval and consent to participate

All animal evaluation was performed with approval from the Ethics Committee of the Affiliated Suzhou Hospital of Nanjing Medical University (K-2023-044).

Declaration of competing interest

The authors declare that they have no known competing financial interests or personal relationships that could have appeared to influence the work reported in this paper.

Acknowledgments

This work was financially supported by the Guangdong-Foshan Joint Fund from Guangdong Basic and Applied Basic Research Foundation (2020B15153000), the Excellent Young Scholars Projects from the National Natural Science Foundation of China (NSFC, 82122002), General Program of NSFC (52335004, 52275199), the Collaborative Research Fund (C5044-21G) and NSFC/RGC Joint Research Scheme (N_PolyU526/22) from the Research Grants Council of Hong Kong, the Innovation and Technology Fund from the Innovation and Technology Commission (ITS/085/21), Beijing Natural Science Foundation (J230001, L248029), and Young Scholars Program of Shandong University.

Appendix. ASupplementary data

Supplementary data to this article can be found online at $\frac{https:}{doi.}$ org/10.1016/j.bioactmat.2025.07.007.

Data availability

Data will be made available on request.

References

- [1] R.M. Baker, L.-F. Tseng, M.T. Iannolo, M.E. Oest, J.H. Henderson, Self-deploying shape memory polymer scaffolds for grafting and stabilizing complex bone defects: a mouse femoral segmental defect study, Biomaterials 76 (2016) 388–398, https:// doi.org/10.1016/j.biomaterials.2015.10.064.
- [2] G. Wang, Z. Lv, T. Wang, T. Hu, Y. Bian, Y. Yang, R. Liang, C. Tan, X. Weng, Surface functionalization of hydroxyapatite scaffolds with MgAlEu-LDH nanosheets for high-performance bone regeneration, Adv. Sci. 10 (2023) 2204234, https://doi. org/10.1002/advs.202204234.
- [3] Y. Zhang, C. Li, W. Zhang, J. Deng, Y. Nie, X. Du, L. Qin, Y. Lai, 3D-printed NIR-responsive shape memory polyurethane/magnesium scaffolds with tight-contact

- for robust bone regeneration, Bioact. Mater. 16 (2022) 218–231, https://doi.org/10.1016/j.bioactmat.2021.12.032.
- [4] J. Delaey, P. Dubruel, S. Van Vlierberghe, Shape-memory polymers for biomedical applications, Adv. Funct. Mater. 30 (2020) 1909047, https://doi.org/10.1002/ adfm.201909047.
- [5] H. Ramaraju, R.E. Akman, D.L. Safranski, S.J. Hollister, Designing biodegradable shape memory polymers for tissue repair, Adv. Funct. Mater. 30 (2020) 2002014, https://doi.org/10.1002/adfm.202002014.
- [6] Q. Ze, X. Kuang, S. Wu, J. Wong, S.M. Montgomery, R. Zhang, J.M. Kovitz, F. Yang, H.J. Qi, R. Zhao, Magnetic shape memory polymers with integrated multifunctional shape manipulation, Adv. Mater. 32 (2020) 1906657, https://doi. org/10.1002/adma.201906657.
- [7] A. Lendlein, H. Jiang, O. Jünger, R. Langer, Light-induced shape-memory polymers, Nature 434 (2005) 879–882, https://doi.org/10.1038/nature03496.
- [8] Z. Tang, L. Guo, M. Xu, H. Ruan, J. Yang, T. Wang, J. Zhang, Q. Wang, Y. Zhang, Tribological behavior of shape memory cyanate ester materials and their tunable friction mechanism, Friction 11 (2023) 1794–1803. https://doi.org/10.1007/s40 544-022-0689-3.
- [9] T. Gong, W. Li, H. Chen, L. Wang, S. Shao, S. Zhou, Remotely actuated shape memory effect of electrospun composite nanofibers, Acta Biomater. 8 (2012) 1248–1259, https://doi.org/10.1016/j.actbio.2011.12.006.
- [10] L.-F. Tseng, P.T. Mather, J.H. Henderson, Shape-memory-actuated change in scaffold fiber alignment directs stem cell morphology, Acta Biomater. 9 (2013) 8790–8801, https://doi.org/10.1016/j.actbio.2013.06.043.
- [11] H.-Y. Yuen, W.-S. Yip, S. To, X. Zhao, Microcurvature landscapes induce neural stem cell polarity and enhance neural differentiation, bio-des, Man 6 (2023) 522–535, https://doi.org/10.1007/s42242-023-00243-5.
- [12] A. Lendlein, S. Kelch, Shape-memory polymers, Angew. Chem., Int. Ed. 41 (2002) 2034–2057, https://doi.org/10.1002/1521-3773(20020617)41:12<2034::AID-ANIE2034>3.0.CO;2-M.
- [13] S. Subramaniam, Y.-H. Fang, S. Sivasubramanian, F.-H. Lin, C.-p. Lin, Hydroxyapatite-calcium sulfate-hyaluronic acid composite encapsulated with collagenase as bone substitute for alveolar bone regeneration, Biomaterials 74 (2016) 99–108, https://doi.org/10.1016/j.biomaterials.2015.09.044.
- [14] H. Yang, N. D'Ambrosio, P. Liu, D. Pasini, L. Ma, Shape memory mechanical metamaterials, Mater. Today 66 (2023) 36–49, https://doi.org/10.1016/j. mattod.2023.04.003.
- [15] H.-P. Bei, X. Ji, T. Xu, Z. Chen, C.-H. Lam, X. Zhou, Y. Yang, Y. Zhang, C. Wen, Y. Liu, X. Zhao, ECM-based Ca²⁺/l-arginine/NO periosteum nourishes bone defect microenvironment, directs macrophage polarity, and accelerates osteogenesis and angiogenesis, Composites, Part B 278 (2024) 111410, https://doi.org/10.1016/j.compositesb.2024.111410.
- [16] T. Xu, Y. Yang, D. Suo, H.P. Bei, X. Xu, X. Zhao, Electrosprayed regenerationenhancer-element microspheres power osteogenesis and angiogenesis coupling, Small 18 (2022) 2200314. https://doi.org/10.1002/smll.202200314.
- [17] Y. Yang, T. Xu, Q. Zhang, Y. Piao, H.P. Bei, X. Zhao, Biomimetic, stiff, and adhesive periosteum with osteogenic-angiogenic coupling effect for bone regeneration, Small 17 (2021) 2006598, https://doi.org/10.1002/smll.202006598.
- [18] Y. Yang, Y. Jia, Y. Zhao, H. Wang, H. Zhang, Recent developments in functional organic polymer coatings for biomedical applications in implanted devices, Friction 12 (2024) 2399–2440. https://doi.org/10.1007/s40544-023-0850-7.
- [19] Y. Zhang, J. Hu, R. Xie, Y. Yang, J. Cao, Y. Tu, Y. Zhang, T. Qin, X. Zhao, A programmable, fast-fixing, osteo-regenerative, biomechanically robust bone screw, Acta Biomater. 103 (2020) 293–305, https://doi.org/10.1016/j. arthip. 2019.12.017
- [20] H. Bhatt, T. Goswami, Implant wear mechanisms—basic approach, Biomed.l Mater 3 (2008) 042001, https://doi.org/10.1088/1748-6041/3/4/042001.
- [21] M.J. Dreyer, B. Weisse, J.I. Contreras Raggio, R. Zboray, W.R. Taylor, S. Preiss, N. Horn, The influence of implant design and limb alignment on in vivo wear rates of fixed-bearing and rotating-platform knee implant retrievals, J. Orthop. Res. 42 (2024) 777–787, https://doi.org/10.1002/jor.25734.
- (2024) 777–787, https://doi.org/10.1002/jor.25734.
 [22] A. Borbely, H.A. Biermann, O. Hartmann, FE investigation of the effect of particle distribution on the uniaxial stress-strain behaviour of particulate reinforced metalmatrix composites, Mater. Sci. Eng. 313 (2001) 34–45, https://doi.org/10.1016/S0921-5093(01)01144-3.
- [23] T. Liu, Z. Wang, D. Zou, A. Zhou, J. Du, Strength enhancement of recycled aggregate pervious concrete using a cement paste redistribution method, Cement Concr. Res. 122 (2019) 72–82, https://doi.org/10.1016/j.cemconres.2019.05.004.
- [24] F. Meng, R.H. Pritchard, E.M. Terentjev, Stress relaxation, dynamics, and plasticity of transient polymer networks, Macromolecules 49 (2016) 2843–2852, https://doi. org/10.1021/acs.macromol.5b02667.
- [25] S. Jiang, J.S.S. Wong, D. Puhan, T. Yuan, X. Bai, C. Yuan, Tribological evaluation of thermoplastic polyurethane-based bearing materials under water lubrication: Effect of load, sliding speed, and temperature, Friction 12 (2024) 1801–1815. htt ps://doi.org/10.1007/s40544-023-0856-1.
- [26] B.C. Tong, A. Barbul, Cellular and physiological effects of arginine, Mini Rev. Med. Chem. 4 (2004) 823–832, https://doi.org/10.2174/1389557043403305.
- [27] J. Rao, X. Mou, Y. Mo, H.-P. Bei, L. Wang, C.Y. Tang, K.-H. Yiu, Z. Yang, X. Zhao, Gas station in blood vessels: an endothelium mimicking, self-sustainable nitric oxide fueling stent coating for prevention of thrombosis and restenosis, Biomaterials 302 (2023) 122311, https://doi.org/10.1016/j. biomaterials.2023.122311.
- [28] Y. Wang, W. Zhai, S. Cheng, J. Li, Surface-functionalized design of blood-contacting biomaterials for preventing coagulation and promoting hemostasis, Friction 11 (2023) 1371–1394. https://doi.org/10.1007/s40544-022-0710-x.

- [29] A.R. Unnithan, A.R.K. Sasikala, B.K. Shrestha, A. Lincoln, T. Thomson, A.J. El Haj, Remotely actuated magnetic nanocarpets for bone tissue engineering: non-invasive modulation of mechanosensitive ion channels for enhanced osteogenesis, Adv. Funct. Mater. 32 (2022) 2201311, https://doi.org/10.1002/adfm.202201311.
- [30] C. Shan, L. Yixuan, S. Rui, M. Xianyi, F. Maximilian, L. Chunguang, K. Katerina, M. Xinyu, W. Jinming, S.-S. Ursula, T. Verena, G. Arne, K. Meik, S. Ulrike, M. Z. Mario, K. Alf, C. Xiaoxiang, S. Georg, B. Aline, L-arginine metabolism inhibits arthritis and inflammatory bone loss, Ann. Rheum. Dis. 83 (2024) 72, https://doi.org/10.1136/ard.2022.23626
- [31] P.S. Ward, C.B. Thompson, Signaling in control of cell growth and metabolism, Cold Spring Harbor Perspect. Biol. 4 (2012), https://doi.org/10.1101/cshperspect a006783
- [32] M. Yu, H. Zhang, B. Wang, Y. Zhang, X. Zheng, B. Shao, Q. Zhuge, K. Jin, Key signaling pathways in aging and potential interventions for healthy aging, Cells 10 (2021), https://doi.org/10.3390/cells10030660.
- [33] Y.-P. Wang, Q.-Y. Lei, Metabolite sensing and signaling in cell metabolism, Signal Transduct. Targeted Ther. 3 (2018) 30, https://doi.org/10.1038/s41392-018-0024-7
- [34] X. Zhao, I. Olsen, H. Li, K. Gellynck, P.G. Buxton, J.C. Knowles, V. Salih, A. M. Young, Reactive calcium-phosphate-containing poly(ester-co-ether) methacrylate bone adhesives: Chemical, mechanical and biological considerations, Acta Biomater. 6 (2010) 845–855, https://doi.org/10.1016/j.actbio.2009.09.020.
- [35] X. Zhao, I. Olsen, J. Pratten, J.C. Knowles, A.M. Young, Reactive calcium-phosphate-containing poly(ester-co-ether) methacrylate bone adhesives: setting, degradation and drug release considerations, J. Mater. Sci. Mater. Med. 22 (2011) 1993–2004, https://doi.org/10.1007/s10856-011-4378-4.
- [36] H. Wang, Y. Yang, W. Zhao, Y. Han, J. Luo, X. Zhao, H. Zhang, Bioinspired polymeric coating with self-adhesion, lubrication, and drug release for synergistic bacteriostatic and bactericidal performance, Adv. Mater. Interfac. 9 (2022) 2200561, https://doi.org/10.1002/admi.202200561.
- [37] S. Neuss, I. Blomenkamp, R. Stainforth, D. Boltersdorf, M. Jansen, N. Butz, A. Perez-Bouza, R. Knüchel, The use of a shape-memory poly(ε-caprolactone) dimethacrylate network as a tissue engineering scaffold, Biomaterials 30 (2009) 1697–1705, https://doi.org/10.1016/j.biomaterials.2008.12.027.
- [38] Q. Zhao, H.J. Qi, T. Xie, Recent progress in shape memory polymer: new behavior, enabling materials, and mechanistic understanding, Prog. Polym. Sci. 49 (2015) 79–120, https://doi.org/10.1016/j.progpolymsci.2015.04.001.
- [39] R. Xie, J. Hu, X. Guo, F. Ng, T. Qin, Topographical control of preosteoblast culture by shape memory foams, Adv. Eng. Mater. 19 (2017) 1600343, https://doi.org/ 10.1002/adem.201600343.
- [40] Q. Zhang, K. Ma, C.-H. Lam, H.-P. Bei, Y. Liu, X. Yang, X. Zhao, Micro- and nano-environment dual-modulated anti-tendon adhesion barrier membranes, Mater. Des. 219 (2022) 110737, https://doi.org/10.1016/j.matdes.2022.110737.
- [41] Y. Yang, T. Xu, H.P. Bei, Y. Zhao, X. Zhao, Sculpting bio-inspired surface textures: an adhesive janus periosteum, Adv. Funct. Mater. 31 (2021) 2104636, https://doi. org/10.1002/adfm.202104636.
- [42] H. Liu, Z. Cai, F. Wang, L. Hong, L. Deng, J. Zhong, Z. Wang, W. Cui, Colon-targeted adhesive hydrogel microsphere for regulation of gut immunity and flora, Adv. Sci. 8 (2021) 2101619, https://doi.org/10.1002/advs.202101619.
- [43] S.-L. Liu, Y.-M. Zhou, D.-B. Tang, N. Zhou, W.-W. Zheng, Z.-H. Tang, C.-W. Duan, L. Zheng, J. Chen, LGR6 promotes osteogenesis by activating the Wnt/β-catenin signaling pathway, Biochem. Biophys. Res. Commun. 519 (2019) 1–7, https://doi.org/10.1016/j.bhrc.2019.08.122
- [44] A. Oryan, A. Kamali, A. Moshiri, M. Baghaban Eslaminejad, Role of mesenchymal stem cells in bone regenerative medicine: what is the evidence? Cells Tissues Organs 204 (2017) 59–83, https://doi.org/10.1159/000469704.
- [45] C. Sonnet, C.L. Simpson, R.M. Olabisi, K. Sullivan, Z. Lazard, Z. Gugala, J.F. Peroni, J.M. Weh, A.R. Davis, J.L. West, E.A. Olmsted-Davis, Rapid healing of femoral defects in rats with low dose sustained BMP2 expression from PEGDA hydrogel microspheres, J. Orthop. Res. 31 (2013) 1597–1604, https://doi.org/10.1002/jor.22407.
- [46] Y. Yang, Q. Zhang, T. Xu, H. Zhang, M. Zhang, L. Lu, Y. Hao, J.H. Fuh, X. Zhao, Photocrosslinkable nanocomposite ink for printing strong, biodegradable and bioactive bone graft, Biomaterials 263 (2020) 120378, https://doi.org/10.1016/j. biomaterials 2020 120378
- [47] W.N. Arifin, W.M. Zahiruddin, Sample size calculation in animal studies using resource equation approach, Malays. J. Med. Sci. 24 (2017) 101–105, https://doi. org/10.21315/mjms2017.24.5.11.
- [48] C. Yang, H. Ma, Z. Wang, M.R. Younis, C. Liu, C. Wu, Y. Luo, P. Huang, 3D printed wesselsite nanosheets functionalized scaffold facilitates nir-ii photothermal therapy and vascularized bone regeneration, Adv. Sci. 8 (2021) 2100894, https://doi.org/10.1002/advs.202100894 printed wesselsite nanosheets functionalized scaffold facilitates nir-ii photothermal therapy and vascularized bone regeneration, Adv. Sci. 8 (2021) 2100894.
- [49] M.L. Bouxsein, S.K. Boyd, B.A. Christiansen, R.E. Guldberg, K.J. Jepsen, R. Müller, Guidelines for assessment of bone microstructure in rodents using micro-computed tomography, J. Bone Miner. Res. 25 (2010) 1468–1486, https://doi.org/10.1002/ jbmr.141.
- [50] T. Wang, J. Bai, M. Lu, C. Huang, D. Geng, G. Chen, L. Wang, J. Qi, W. Cui, L. Deng, Engineering immunomodulatory and osteoinductive implant surfaces via mussel adhesion-mediated ion coordination and molecular clicking, Nat. Commun. 13 (2022) 160, https://doi.org/10.1038/s41467-021-27816-1.
- [51] Y. Yang, T. Xu, H.P. Bei, Y. Zhao, X. Zhao, Sculpting bio-inspired surface textures: an adhesive janus periosteum, Adv. Funct. Mater. 31 (2021) 2104636, https://doi. org/10.1002/adfm.202104636.